Supplementary Material

We provide additional data and specifications that we use to support the statements in the main text.

The Supplementary Material is organized as follows:

- **A: Description of additional experiments**
- **B: Heat transfer model**
- **C: Figures for Methods**
- **D: Description of Supplementary Movies**
- **E: Table of fluidic setup details**
- **F: References in Supplementary Material**

A: Description of additional experiments and characterizations

This section contains the description of additional experiments and characterizations peformed to support the results in the main text, and is divided in the following sections:

1. **Evaluating vapor pressure of the LBF**
2. **Dependency of maximum pressure on the amount of Novec 7000®**
3. **Ideal thermopneumatic cycle using manual valves**
4. **Accuracy of air volumes and the recovery of initial condition during consecutive thermopneumatic loops**
5. **Characterization of pressure-release valve opening pressures with varying thickness**
6. **Efficiency calculations**
7. **Energy density, power density, and efficiency comparison**
8. **Comparison with other LBF candidates**
9. **Strategies to reduce potential leakages of LBF**

A.1: Evaluating vapor pressure of the LBF

Given the interest in working with temperatures in the range compatible with real-world external temperatures and meaningful pressures in the context of soft robotics, we use the Clausius-Clapeyron relation for vapor pressure of the LBF. We show that this relation sets a theoretical constraint on the potential in energy harvesting for our thermopneumatic unit.

First, we consider the LBF undergoing a phase transition and assume that the LBF is at its vapor pressure $p_{\text{vap, A}}$ when at boiling temperature $T_{\text{boil, A}}$. Through the Clausius-Clapeyron

equation, we derive the boiling temperature $T_{\text{boil, B}}$ for another corresponding vapor pressure $p_{\text{vap, B}}$ when the latent heat of vaporization of the fluid L is known

$$p_{\text{vap, B}}(T_{\text{boil, B}}) = p_{\text{vap, A}} \cdot \exp\left[-\frac{L}{R}\left(\frac{1}{T_{\text{boil, B}}} - \frac{1}{T_{\text{boil, A}}}\right)\right] \tag{S1}$$

with R the gas constant. Through Equation S1, it is possible to infer the vapor pressure p_{vap}, namely the maximum pressure that an evaporating fluid can reach at a given temperature before the coexistence of fluid and gas phase at thermal equilibrium. Once the vapor pressure is reached and the system is at equilibrium with its environment, no further increase in pressure can occur.

For our application, this means that once the LBF has reached its vapor pressure, a pressure increase can occur only if the temperature is further increased, consequently increasing the vapor pressure according to Equation S1. We overlay the results from Clausius Clapeyron equation with experimental data in Figure 3**b**. Equation S1 returns the ideal behaviour of the LBF of our choice, whereas our experimental data encloses the response of the different subsystems in our design. Deviations between experimental data and the results of Equation S1 can be justified by the presence of air inside the air reservoir that causes an increase in pressure upon heating up, even before the evaporation of the LBF.

A.2: Dependency of maximum pressure on the amount of Novec 7000®

To better understand how a different amount of LBF (Novec 7000®) in the TPU pouch affects the scaling of maximum pressure for a given air reservoir volume and maximum temperature in the system, we perform a comparative experiment in Figure S1. We consider the same plastic bottle as an air reservoir as the one we used to perform our experiments in Figures 1-2, with no valves connected to it and place the system in the oven while controlling its air pressure and temperature. We increase the temperature from $T_{\text{lab}} = 27°\text{C}$ to $T_{\text{max}} = 55°\text{C}$ before letting the system thermalize back to T_{lab}. In Figure S1**a**, we report the measured pressure as a function of the oven temperature in time for different amounts of LBF, compared with the case with no

LBF-pouch inside the bottle. At the same time, we plot the vapor pressure p_{vap} of the Novec 7000® LBF to compare our experimental results with data from the technical datasheet of the LBF.

$$p_{\text{vap}}(T) = e^{\frac{-3548.6}{T}+22.978} \tag{S2}$$

This visualization suggests that, although there is a small discrepancy of the temperatures of maximum pressures between experimental data and p_{vap} fit from the datasheet (Equation S2), the evaporation of the LBF returns maximum pressures comparable with the ones indicated on the datasheet for given maximum temperatures. We justify deviations between the two by considering that the expression in Equation S2 suggested by the datasheet of Novec 7000® is a fit performed on the LBF alone, whereas we consider temperature sweeps happening in the isolated bottle with LBF-pouch inside and at steady state. We expect the presence of air inside the air reservoir to cause deviations from the ideal LBF thermopneumatic response. Following the method we described in Equation 4, in Figure S1**b** we report the value of the pressure against $V(p)$ for the different realizations of our experiment with different LBF and observe that the compression ratio we obtain increases with higher peak pressures, i.e. amount of LBF fluid in the compliant pouch.

We report the time response of the pressure to the temperature cycle for the different amounts of LBF fluid in Figure S1**c**. For these experiments, as well as for the ones performed while gathering the data for Figure 1-2, the oscillations in temperature happening close to the target T_{max} value are the result of the PID controller of the oven as the temperature inside the oven chamber approaches the desired end value. We do not observe these oscillations during the cooling down process as, to allow gradual decrease in temperatures, we switch off the oven while leaving its door closed. This means that, during the cooling down, the PID controller of the oven cannot intervene in regulating the temperature and we use the oven hardware to passively regulate the temperature back to T_{lab} slowly.

This experimental realization clearly shows that using the LBF-pouch inside the air reservoir can increase the maximum pressure reached by the system upon pressurization by more than 500% by increasing the amount of LBF. However, a limiting factor for the maximum pressure that the system can reach, besides mechanical failures that might occur at higher pressure, is the p_{vap} vapor pressure of LBF. As we explained while describing our model in Figure 3, vapor pressure sets a thermodynamic boundary for further evaporation of the LBF once evaporation of the LBF occurs, thus limiting the potential for reaching higher pressure for a set maximum temperature.

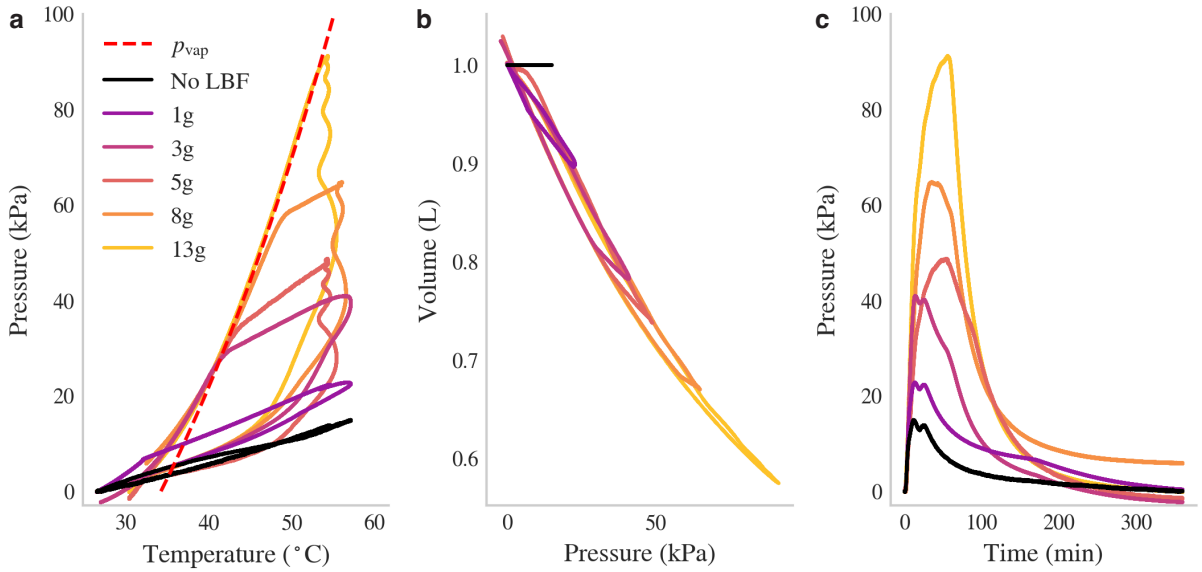

Figure S1: **Characterization of the thermopneumatic pressure response as a function of the LBF mass in the pouch.** We consider different LBF amounts and compare the thermopneumatic response of the system with the case where no LBF fluid is used inside the pouch (black solid lines). **(a)** Pressure as a function of air temperature. We report the vapor pressure p_{vap} using the red dashed line. **(b)** Volume as a function of pressure, evaluated using Equation 4. For the case with no LBF in the pouch, we assume that the geometrical deformation of the air reservoir is negligible so that air molecules fully occupy the air reservoir volume of 1L. **(c)** Pressure in time for the different scenarios investigated.

A.3: Ideal thermopneumatic cycle using manual valves

Our data in Figure 1 suggests that the non-zero closing pressures, both of our pressure-release valve and of the one-way valve, limit the pneumatic response of our thermopneumatic approach. At the same time, this feature hinders both the efficiency and the recharging dynamic of the energy-harvesting cell. To better explore the differences between our experimental realization of our thermopneumatic strategy with an ideal experimental setup with zero closing pressure, we perform a comparative experiment by using the same TPU pouch with LBF as in Figure 1, but replacing the commercial one-way and custom pressure-release valves in Figure S17**a** with manual FESTO valves.

With this experiment, we mean to emulate experimentally the thermopneumatic response of our system under the hypothesis of ideal (with zero closing pressure) one-way and pressure-release valves. While performing this experiment, we regulate the oven to the same maximum temperature as the one we used in Figure 1**b-d**. At the same time, for a better comparison, we use the same equations and protocols to infer the change in volumes inside the air reservoir as in Equations 4-7.

To perform this experiment, we initialize the system at temperature $T_{\text{lab}} = 27°\text{C}$ and place the air reservoir in the oven before initializing the same temperature profile for the oven we used in Figure 1. When the pressure reaches approximately the opening pressure of the pressure-release valve, we emulate the opening of the pressure-release valve by opening the manual valve at the outlet. Similarly, after the discharge phase, we close the manual valve at the outlet before switching off the heating from the oven (2 hours after the beginning of the experiment) while opening the manual valve at the inlet of the energy-harvesting cell. We then let the experiment run for the remaining 8 hours during which the temperature slowly drops up until T_{lab}, just like in Figure 1**c**-**d**.

Data from this experiment is shown in Figure S2, and indicates two main features of such

an ideal system. First, the LBF in the TPU pouch can expel air volume up to the point where the air pressure equals ambient pressure, thus producing a larger hysteresis in the pressure-volume plane and yielding more work and higher efficiency. Secondly, we observe that by integrating the airflow during the recharge phase, we fully recover the initial state of this experimental realization.

In conclusion, this comparative experiment that emulates the thermopneumatic response in the case of ideal valves with zero closing pressures serves two purposes. First, it indicates that the data processing method we use is able to grasp the expected behavior of an ideal system, showing also that the integration technique we used and the workflow are reliable enough. Secondly, it suggests that the initial state of pressure and volume in the system is not fully recovered due to the non-zero closing pressure of the one-way valve, predominantly. This also means that, upon consecutive thermopneumatic cycles, slightly fewer air molecules are reinjected in the air reservoir during the recharge phase.

A.4: Accuracy of air volumes and the recovery of initial condition during consecutive thermopneumatic loops

Especially while considering the experiments in Figure 2, it is worth mentioning that there is a significant difference between the discharge (10 minutes) and recharge (3 hours) times. This places notable challenges on the precision and comparison between some of the measurements. We show details of the raw data from the new flow sensors in Figure S3. This difference in time scales introduces non-trivial challenges while collecting the voltage readings of the flow sensor and performing the time integration of the SLPM to infer the geometrical volume of air in time using Equation 7. However, our protocol for executing the experiments and processing sensor data seems to be sufficiently accurate to represent an ideal thermopneumatic cycle as shown in previous section.

We believe that the mismatch in air volumes measured at the beginning and at the end of

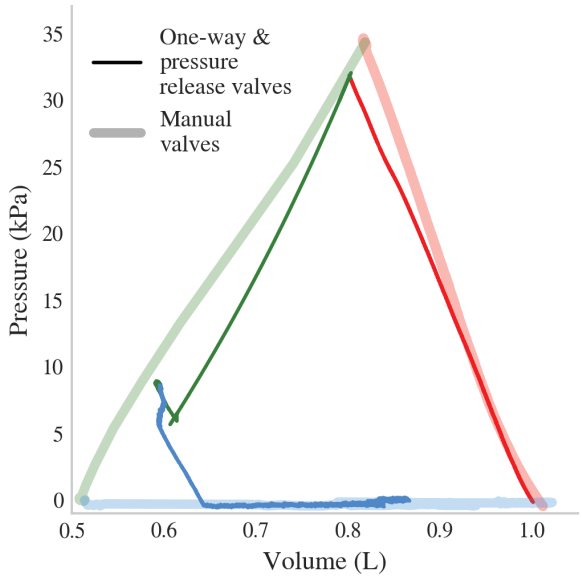

Figure S2: **Comparison of the heat cycle using valves and manual control**. The thin line shows the heat cycle obtained from the experiment performed using the combination of pressure release and one-way valve as in our thermopneumatic cell from Figure 1**c**. The thicker line indicates results from the experiment performed using manually operated valves, to simulate zero closing pressures both on the pressure-release and one-way valve. We highlight in red, green, and blue the compression, discharge, and recharge phases respectively for the two cases.

an energy harvesting cycle is not caused by measurement-related errors. In particular, we do not deem systematic integration error to dramatically affect our results, as we do not observe a drift in flow data over time, and it appears the flow sensor recovers its offset zero value at the beginning of each new thermal cycle. On top of that, we report that the commercial Luer® one-way valves we performed our experiments with have low but non-zero opening and closing pressures that could prevent the full recovery of air volume after the recharge phase. We highlight that our pressure measurements indicate that the opening and closing pressures do not drift in time, suggesting that the pneumatic behavior of our custom-made component is stable upon repeated energy harvesting cycles. As a one-way valve, we use a commercial Luer® duckbill check valve.

At the same time, we observe a slight pressure drop just after each of the discharge phases, as

we observe in the insets of Figure 2**a**. We further investigate these pressure drops in Figure S4. In Figure S4**a**, we report the average value and standard deviation of the equilibration pressure measured for the end of the discharge phase up until the oven is switched off. In Figure S4**b**, we show the deviation of the average equilibration pressures after the firing event measured in Figure S4**a** from the first thermopneumatic cycle. We evaluate the difference in average equilibration pressure between consecutive thermopneumatic loops in Figure S4**c**. From this data, we observe a loss in pressure after the firing event that stabilizes at about 0.5kPa/cycle after five thermopneumatic cycles. Although we acknowledge the potential leakage of LBF from the TPU pouch as a potential cause for this slight drop in equilibration pressure through loss of powering fluid over time, we believe a more realistic explanation lies in the non-zero closing pressure of the one-way valve. While reproducing our energy harvesting approach using manual valves instead of the custom pressure-release valve, we observe that the system is indeed able to recover its initial state.

In conclusion, even though the volume measurements might not be accurate due to the experimental challenges, experimental data suggest that our protocol to infer air volumes is still accurate enough to grasp the slight variation in performance of the energy harvesting unit over time.

A.5: Characterization of pressure-release valve opening pressures with varying thickness

We investigate how the silicone dome geometry affects the critical pressure of the pressure-release valve, particularly focusing on its thickness. We fabricate different silicone domes and report their fluidic properties in Figure S5. We fabricate domes with different thicknesses $t = [0.75, 1, 1.25, 1.5, 1.9]$mm and sweep input air pressure from p_{amb} to $p_{\text{max}} = [5, 10, 15, 30, 50]$kPa while measuring the airflow. We then measure Δp_{open} (Δp_{close}) the pressure at which the valve transitions from 0 to 0.05SLPM (0.05 to 0.0SLPM).

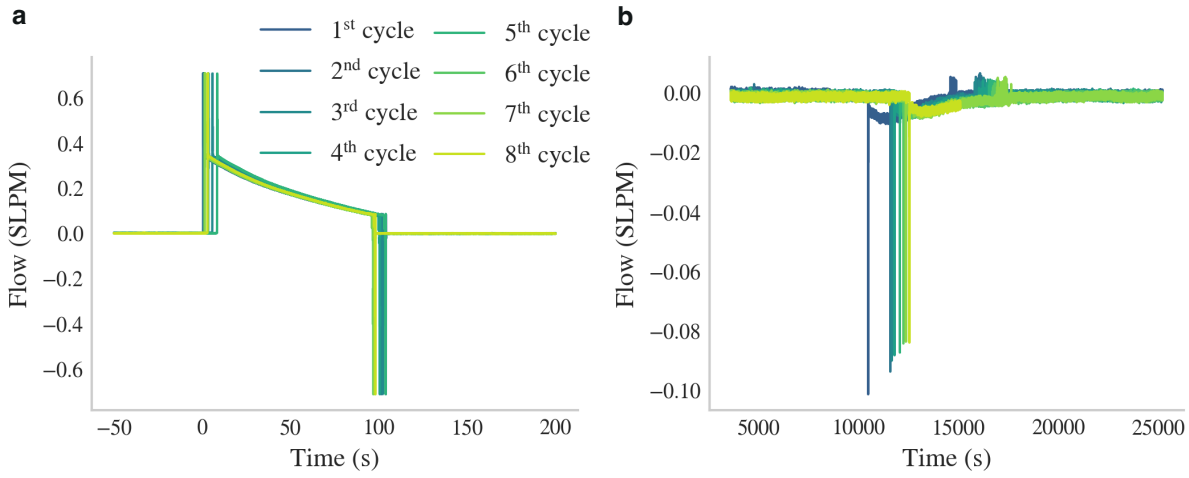

Figure S3: **Additional data for the flow measurements performed during the experiment in Figure 2 on repeated energy harvesting cycles.** **(a)** Flow data for the discharge phase. We overlay the different thermopneumatic cycles in time to highlight that the discharge phases we measured always follow the same trend in time and have well-determined duration. **(b)** Highlight of the incoming net flow during the recharge phase.

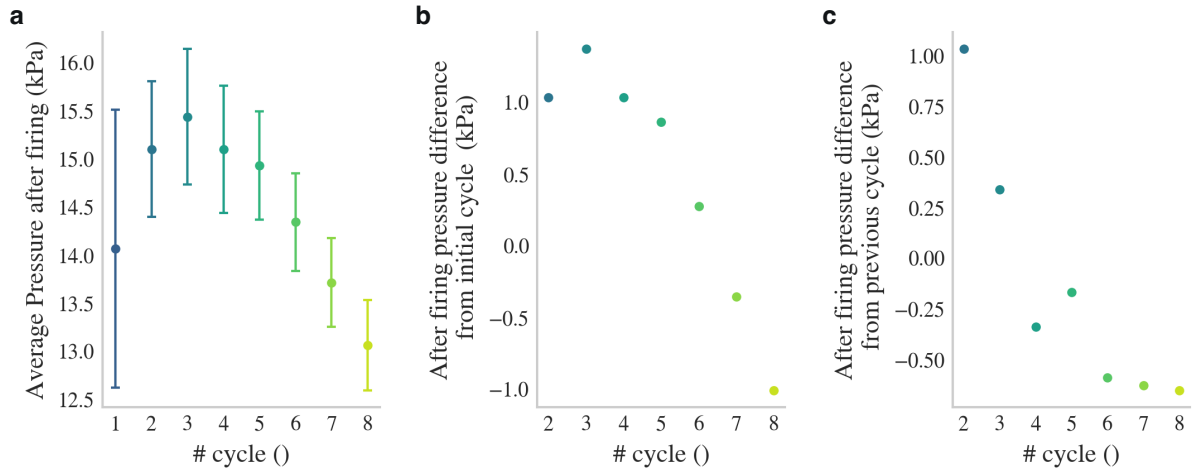

Figure S4: **Characterization of pressure losses upon repeated thermopneumatic cycles.** We characterize the pressure losses from the time instance where the pressure-release valve closes up to when we switch off the heating in the controlled oven environment and consider its average and standard deviation value for the different thermopneumatic cycles in Figure 2. **(a)** Equilibration pressure per cycle with error bar representing its standard deviation. **(b)** Difference of average equilibration pressures with the first thermopneumatic cycle. **(c)** Difference between the average equilibration pressures of consecutive thermopneumatic cycles.

For each dome thickness, we pressurize the valves 30 times and report the average and standard deviation of the opening and closing pressures from the last 15 pressurization and depressurization cycles. From our experiments, we observe a non-linear increase of the opening pressures with increasing dome thickness of the dome structure, the closing pressures follow a mostly linear trend. Therefore, for what concerns our purposes, we observe that the dome thickness can be used as a control parameter to embed different pneumatic behaviors in fluidic, electronics-free circuits.

To maximize the volume spanned by the thermodynamic state of the energy harvesting unit in the pressure-volume space, it is crucial to use a pressure-release valve with the largest discrepancy between opening and closing pressures that can be triggered using real-world conditions. Therefore, in our study, we focused on the silicone dome design with thickness $t = 1.90$mm.

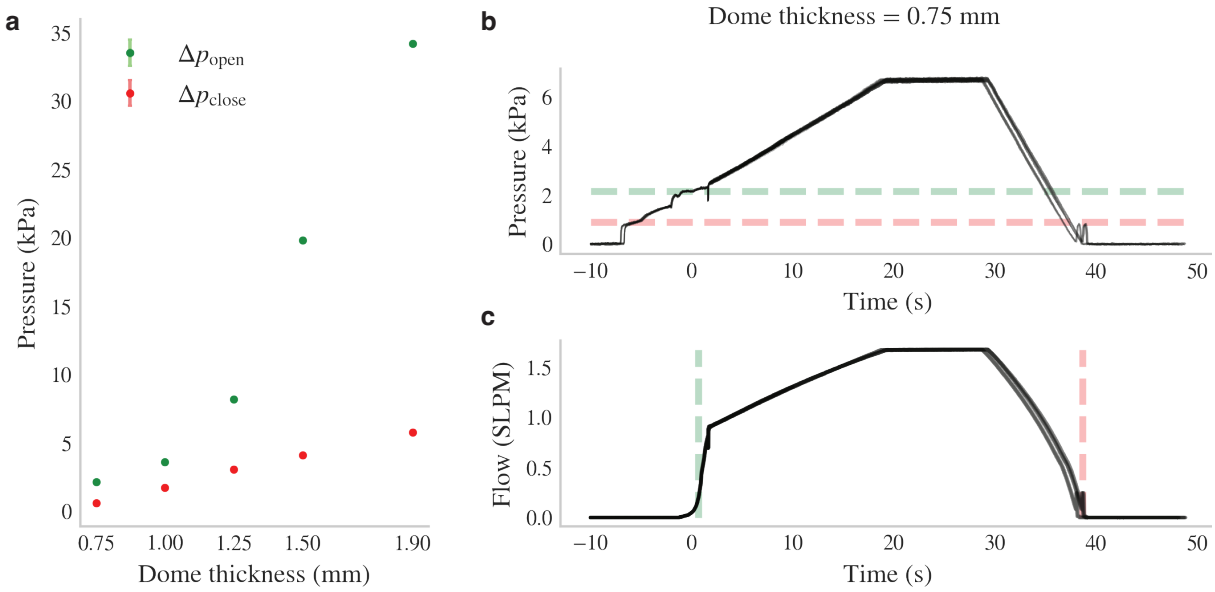

Figure S5: **Effect of dome thickness on opening and closing pressures of the pressure-release valve. (a)** Opening and closing pressures for different thicknesses tested. Error bars (standard deviation) are reported but not visible. **(b-c)** Example of characterization data through overlay of **b** pressure and flow **c** in time for 15 consecutive pressurization and depressurization cycles for $t = 0.75$mm. We highlight the measured opening and closing pressure values with the corresponding flow measured with the green and red dashed lines, respectively.

A.6: Efficiency calculations

With the goal in mind to evaluate the efficiency of our thermopneumatic approach and quantify the performance of our energy harvesting cell compared to already developed technologies, we consider the following hypotheses. We particularly focus on the experimental results from Figure 1, thus we perform our analysis considering that the energy harvesting cell operates between $T_{\text{lab}} = 27°\text{C}$ and $T_{\text{max}} = 43°\text{C}$.

For our analysis, we can consider that the TPU pouch containing the LBF operates as a thermally activated piston that compresses and pressurizes the air volume inside the air reservoir upon evaporation of the LBF. We focus on the efficiency of one full thermopneumatic cycle. This hypothesis allows us to approximate, over one thermopneumatic cycle, the change in internal energy is neglible, that is $\Delta U = 0$. This means that we can evaluate the efficiency η of our thermopneumatic approach by considering

$$\eta = \frac{|W|}{Q_{\text{in}}} = \frac{Q_{\text{in}} - |Q_{\text{out}}|}{Q_{\text{in}}} = 1 - \frac{|Q_{\text{out}}|}{Q_{\text{in}}} \tag{S3}$$

We consider this approximation realistic in the first-order approximation and evaluate the work W done by the system on its surroundings, following from the first law of thermodynamics, as equal to the net heat exchanged (Q_{in} input heat and Q_{out} output heat) by the system during one thermopneumatic cycle $W = Q_{\text{in}} - |Q_{\text{out}}|$. However, including heat losses during the separate thermodynamic processes is a non-trivial task while modeling our thermopneumatic approach, as they are related to the specific trajectory in the thermodynamic space, together with different timescales of phase transitions, thermal cycles, and material properties simultaneously. Therefore, we simplify our analysis by considering the ideal (lossless) behavior of such phenomena to simplify both the description and modeling, aware that our calculations will only be able to yield a theoretical upper limit for efficiency.

In our model, we choose to approximate the complex polytropic processes in the thermop-

neumatic processes with useful simplifying assumptions that we summarize here. Including a more detailed model, e.g., with a detailed description of phase transitions, would still require complex approximations and fitting of physical parameters that are not often accessible experimentally. Instead, we prefer to focus on outlining the main contributions to heat transfer and infer a first-order estimate for efficiency.

To evaluate the heat exchange over one thermopneumatic cycle, we study the compression, discharge, and recharge phases separately. For the remainder of this section, we will indicate them as processes 1, 2, and 3, respectively.

1. During the compression phase, we define $Q_{1,\,\mathrm{air}}$ as the heat needed to bring the temperature of the mass of air inside the air reservoir from T_{lab} to T_{max}. As we know the volume of the reservoir, assuming the volume of the pouch is initially negligible with respect to the air reservoir volume, we can evaluate the heat $Q_{\mathrm{air},\,1} = m_{\mathrm{air},\,1} c_{\mathrm{air}} (T_{\mathrm{max}} - T_{\mathrm{lab}})$, being $m_{\mathrm{air},\,1} \simeq 1.29\mathrm{g}$, mass of $1L$ of air at ambient pressure and T_{lab} and ambient pressure p_{amb}.

   Conversely, the increase in pressure is obtained as a consequence of heating up, and then evaporation of the LBF. We separate the $Q_{\mathrm{LBF},\,1}$ contributions in $Q_{\mathrm{LBF},\,1,\,T_{\mathrm{lab}} \to T_{\mathrm{PT}}}$, $Q_{\mathrm{LBF},\,1,\,\mathrm{PT}}$ and $Q_{\mathrm{LBF},\,1,\,T_{\mathrm{PT}} \to T_{\mathrm{max}}}$ as the heats required to heat from lab temperature to the boiling point, to evaporate and then to bring the LBF gas to maximum temperature. We observe experimentally that evaporation (condensation) starts to occur already at temperatures lower (higher) than the phase transition temperature for a given pressure of the fluid. We justify this observation by speculating that the LBF molecules have to observe a Maxwell-Boltzmann distribution of velocities and that the phase transition, especially due to the contextually increasing/decreasing pressures of the LBF, is not sudden. Considering the small masses of LBF we use in our experiments, we assume the phase transitions happens in a fast time scale. At the same time, we approximate the phase transitions to occur at $T_{PT}(p_{\mathrm{amb}}) = 34^{\circ}\mathrm{C}$, even when pressure is higher than ambient pressure. Nevertheless,

for simplicity of the model, we model phase transitions to occur at once when the system reaches the transition temperature of $T_{\text{PT}}(p_{\text{amb}})$.

To raise the temperature of a mass m_{LBF} of LBF up to its boiling point and starting from T_{lab}, we consider the LBF specific heat c_{LBF}, so that

$$Q_{\text{LBF, 1, } T_{\text{lab}} \to T_{\text{PT}}} = m_{\text{LBF}}\ c_{\text{LBF}} \cdot \big(T_{\text{PT}}(p_{\text{amb}}) - T_{\text{lab}}\big) \tag{S4}$$

To evaporate the mass of LBF at $T_{\text{PT}}(p_{\text{amb}})$, the environment must provide heat $Q_{1\text{ LBF, PT}}$ so that, given the heat of vaporization of the LBF L

$$Q_{\text{LBF, 1, PT}} = m_{\text{LBF}} \cdot L \tag{S5}$$

We assume that once $Q_{\text{LBF, 1, PT}}$ is provided to the system at $T_{\text{PT}}(p_{\text{amb}})$, all LBF molecules evaporated, upon further increase of temperature up to T_{max}, can be achieved if $Q_{\text{LBF, 1, } T_{\text{PT}} \to T_{\text{max}}}$ is provided to the system, with

$$Q_{\text{LBF, 1, } T_{\text{PT}} \to T_{\text{max}}} = m_{\text{LBF}}\ c_{\text{LBF}} \cdot \big(T_{\text{max}} - T_{\text{PT}}\big) \tag{S6}$$

From the aforementioned equations, we infer that there is a minimum amount of heat required in order to bring the system from its initial condition up to the end of the compression phase $Q_1 = Q_{\text{LBF, 1}} + Q_{\text{air, 1}}$ where

$$Q_{\text{LBF, 1}} = Q_{\text{LBF, 1, } T_{\text{lab}} \to T_{\text{PT}}} + Q_{\text{LBF 1, PT}} + Q_{\text{LBF, 1, } T_{\text{PT}} \to T_{\text{max}}} \tag{S7}$$

$$= m_{\text{LBF}} \Big(c_{\text{LBF}} \big(T_{\text{PT}} - T_{\text{lab}}\big) + L\ + c_{\text{LBF}} \big(T_{\text{max}} - T_{\text{PT}}\big) \Big) \tag{S8}$$

$$= m_{\text{LBF}} \Big(c_{\text{LBF}} \big(T_{\text{max}} - T_{\text{lab}}\big) + L \Big) \tag{S9}$$

from which we infer that, given our approximations, the exact temperature at which the phase transition of the LBF occurs does affect the heat balance of the LBF during the compression phase.

2. We assume the discharge phase to occur fast enough compared to the timescales of compression and recharge phase. This observation is supported by data in Figure S17**b** and Figure S3 where we observe that while the discharge and recharge phase have a duration in the order of hours, the discharge phase happens in about 100 s. We use this observation to model the discharge as an adiabatic, fast discharge of air molecules through the load. In addition to that, within our sensing resolution, the discharge process does not produce measurable effects on the air temperature inside the air reservoir. This approximation of adiabatic discharge can be considered valid up until the load connected to the output of the pressure-release valve is not large enough to slow down the discharge phase to time scales comparable with the heat exchange processes.

   Therefore, when focusing on the heat exchange that we aim to model and use to evaluate the efficiency in Equation S3, we assume that no heat is exchanged during the discharge phase. The only thermodynamic consequence of the discharge we consider is that air molecules are expelled until the closing pressure is reached.

   Starting from our experimental data and ideal gas law, we can compute the mass of air inside the air reservoir just at the end of the discharge process. When considering that at the end of the discharge phase (closing of the pressure-release valve), the air inside the air reservoir has pressure $\Delta p_{\text{close}} \simeq 11\text{kPa}$, volume $.6\text{L}$ and temperature $T_{\text{discharge}} = 43^{\circ}\text{C}$, we can derive from ideal gas law that the number of molecules in the system is $m_{\text{air, 2}} \approx 0.8\text{g}$. If we compare this mass with the initial air $m_{\text{air, 1}} \approx 1.3\text{g}$ obtained following the same procedure, we observe that almost one-third of the air mass is expelled as a consequence of the discharge phase.

3. For computing the heat exchanged during the recharge phase, we consider that the preserved amount of LBF has to undergo ideally the inverse of the processes we described

in process 1. This means that the LBF undergoes cooling down up to the condensation temperature and condensation, before reaching the initial temperature T_{lab}. Thus, from a thermodynamic point of view, we assume that the amount of heat exchanged during this process, for what concerns the LBF, is $Q_{\text{LBF, 3}} = -Q_{\text{LBF, 1}}$.

At the same time, for what concerns the air inside the air reservoir during the recharge phase, we observe that as the air cools down, it returns heat to the environment around the energy harvesting unit, before recharging air molecules through the one-way valve. This is mostly because the actual recharge can only take place when the pressure inside the air reservoir is lower than ambient pressure. We assume that such a condition can only manifest after the condensation of the LBF has occurred, as observed in Figure 1**d**. This means that during the recharge phase, the $m_{\text{air, 2}}$ mass of air is releasing energy to the environment while cooling down from $T_{\text{discharge}} = 43°\text{C}$ to T_{lab}, returning to the environment

$$Q_{\text{air, 3}} = m_{\text{air, 2}} c_{\text{air}} \left(T_{\text{lab}} - T_{\text{discharge}} \right) \tag{S10}$$

Therefore, the actual air molecule recharge is instantiated by this slightly negative pressure generated by the condensation of the LBF. From a thermodynamic point of view, this process can be regarded as an isobaric expansion of the air at ambient pressure and temperature.

When considering the results of the individual processes, we can obtain an upper limit for the efficiency of the system from Equation S3

$$\eta = 1 - \frac{|Q_{\text{LBF, 3}} + Q_{\text{air, 3}}|}{Q_{\text{LBF, 1}} + Q_{\text{air, 1}}} \tag{S11}$$

$$= 1 - \frac{m_{\text{LBF}}\Big(c_{\text{LBF}}\big(T_{\text{max}} - T_{\text{lab}}\big) + L\Big) + m_{\text{air, 2}}c_{\text{air}}\big(T_{\text{lab}} - T_{\text{discharge}}\big)}{m_{\text{LBF}}\Big(c_{\text{LBF}}\big(T_{\text{max}} - T_{\text{lab}}\big) + L\Big) + m_{\text{air, 1}}c_{\text{air}}(T_{\text{max}} - T_{\text{lab}})} \tag{S12}$$

Given our experimental conditions with $m_{\text{air}} = 0.0013$kg, $m_{\text{LBF}} = 0.005$kg and considering that $c_{\text{air}} = 700$ J/(kg·K), $c_{\text{LBF}} = 1300$ J/(kg·K), $L = 142000$J/kg, we obtain an upper theoretical value for efficiency in our experiment of $\eta = 0.87\%$, $\eta_{\text{Carnot}} = 5.06\%$, so that $\frac{\eta}{\eta_{\text{Carnot}}} = 0.172$. We report the scaling of η as a function of m_{LBF} in Figure S6.

For the aforementioned reasons, provided that the discharge phase is considered adiabatic, our approximations return an upper boundary for efficiency, irrespective of the load used to evaluate the efficiency of the thermopneumatic cycle. This also means that the work done on the environment by the pressurized air is independent of the loading conditions (trajectory in the pressure-volume plane), as is known in adiabatic processes.

Furthermore, we evaluate the theoretical lower bound for efficiency, based on the following arguments. First, we consider that when our system reaches the firing threshold, there is a minimal amount of work that it performs which is to expel a $\Delta V_{\text{firing}} \simeq 0.2$L volume of air while decreasing its internal pressure by $\Delta p_{\text{firing}} = p_{\text{open}} - p_{\text{open}} = 26$kPa. Therefore, the minimal work that the system can perform is $W_{\text{min}} = \Delta V_{\text{firing}} \Delta p_{\text{firing}} \simeq 2.7J$, that we estimate from the area in the pressure-volume curve between the beginning and end of the discharge phase in Figure 1**c**. As for the minimal required input energy to bring the system to the discharge phase, we consider the ideal case in which the starting temperature is the boiling temperature of the LBF at ambient pressure ($T_{\text{boil}}(p_{\text{amb}}) = 34°$C). As maximum operating temperature, we consider the T_{max} from our experiment in Figure 1 $T_{\text{max}} = 42°$C. When considering $Q_{\text{LBF,1}}$ heat related to the compression phase for the LBF, we have to take into account the energy to let its temperature

increase within the operating ranges and the latent heat of vaporization, as we described in Equation S9. For the air in the reservoir, we only consider $Q_{\text{air,1}}$ heat required to heat it from $T_{\text{boil}}(p_{\text{amb}})$ to T_{max}, given the air mass and heat capacity. Using these operating temperatures and repeating the calculations for the input energy $Q_1 = Q_{\text{LBF,1}} + Q_{\text{air,1}}$ heat. From our calculation, we derive a lower bound of 0.38% when using $m_{\text{LBF}} = 0.005$g. Based on these calculations, in Figure S6**a** we report the scaling of the theoretical lower bound of efficiency with increasing mass of the LBF.

As we argue in Supplementary Material A6, incorporating more detailed hypotheses that, e.g, explicitly resolve phase transitions, would still entail substantial approximations. On top of that, it would also require the calibration of such additional physical parameters that are often not measurable in experiments. The same arguments apply when studying a lower bound for the efficiency, besides the trivial $\eta \geq 0$.

Determining a realistic efficiency value experimentally would require a substantially more advanced experimental setup. This setup would need to integrate our thermal regulation, pneumatic, and thermal measurements with calorimetry (e.g., a bomb calorimeter or heat flux meters). Moreover, adding more detailed hypotheses (e.g., explicitly resolving phase transitions) would still rely on significant approximations and introduce additional parameters that are difficult to access experimentally.

A.7: Energy density, power density, and efficiency comparison

Only a few publications report data concerning the weight, energy, and power of the implementations in their studies. This means that only a few data points are available, compared to case studies where, e.g., the cost of transport is investigated. When data is available, we compare the claimed efficiency for the same publications, in order to have a metric to compare overall performances (Figure S7. This investigation is generally disregarded in the field. When com-

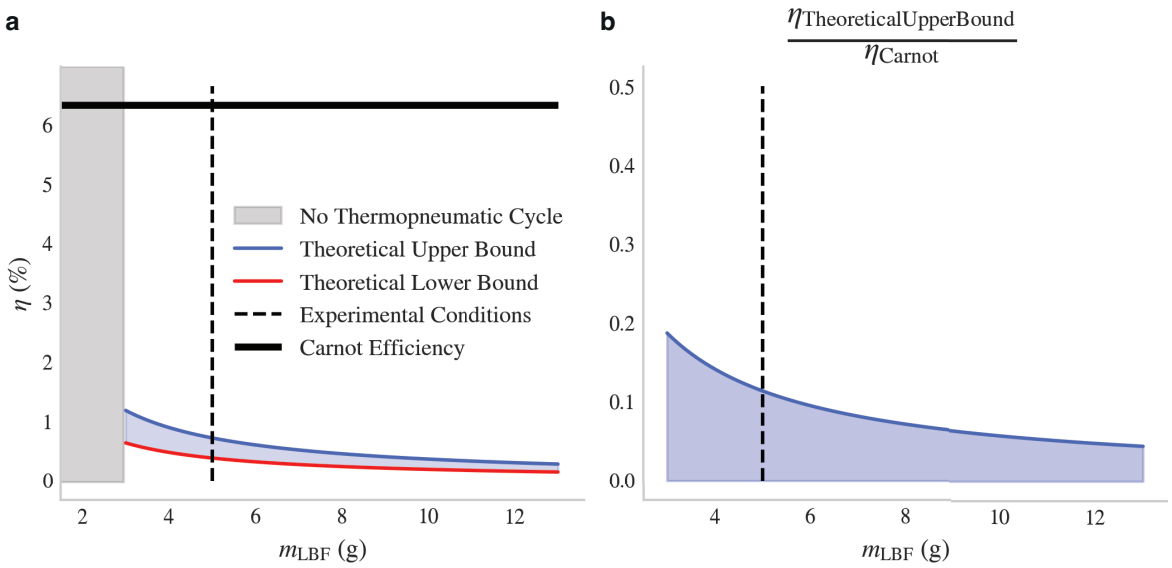

Figure S6: **Model for theoretical upper bound efficiency, lower bounds of efficiency and Carnot efficiency for different mass of LBF (m_{LBF}).** **(a)** Comparison of theoretical upper and lower bounds with corresponding Carnot efficiency. We highlight in blue the allowed values of efficiency for its corresponding m_{LBF} value. With the dashed vertical black line we highlight $m_{\text{LBF}} = 5$g, since we used this amount in our experiments. The gray area indicates m_{LBF} values for which, according to our experiments in Figure S1, the opening pressure of $\Delta p_{\text{open}} = 33$kPa is not reached, hence not of interest for our investigation on efficiency. **(b)** Comparison of theoretical upper bound for efficiency in our system over the correspondent Carnot efficiency.

paring the efficiency of our system with the reported efficiency in different strategies, we use the theoretical upper limit of 1% for our case study.This decision is justified by the consideration that, unlike in case studies where the energy input can be determined with relative ease (for instance by knowing the enthalpy in a chemical reactor, by assuming adiabatic discharge conditions for pressurized canisters, or by integrating power consumption over time in an electrical battery) the direct experimental quantification of heat fluxes is substantially more challenging. In particular, heat exchange processes often involve complex boundary conditions, temperature gradients, and transient phenomena, all of which complicate accurate measurement and require more sophisticated instrumentation and analysis. As an example, calorimetric bombs and heat flux transducers would enable such measurements, thus allowing us to verify our theoretical

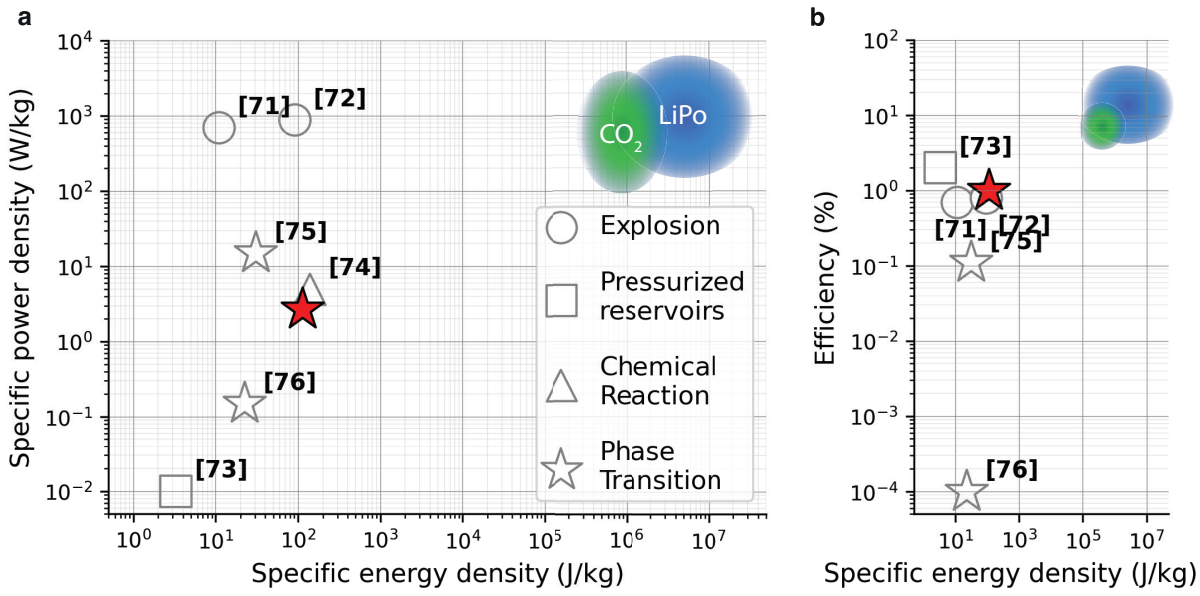

Figure S7: **Comparative study on literature examples for specific energy density, specific energy density, and efficiency to power energy autonomous soft robotic systems.** We compare our results to available experimental data from different energy sources [2, 3, 4, 5] and phase-transition driven powering strategies [6, 7]. On top of that, we report metrics for LiPo batteries and CO_2 canister [8] in blue and green, respectively. With the red star, we report the extracted metrics from the upper theoretical limit in our case study. The efficiency we report is the upper threshold for the efficiency we study in Figure S6. In (**a**), we evaluate the power density using the discharge time of $\sim$ 40s we have observed in the indoor locomotion experiment. For the publication leveraging chemical reactions (triangle), no data was reported about efficiency.

approximation.

When an energy harvesting device is presented, we observe from the literature that devices capable of extracting energy from their environment, e.g., by incoming radiation [50, 7], use it to directly perform work. Instead, in our case, we separate the energy accumulation and energy release phases through consecutive, non-simultaneous, compression and discharge phases. We include in Figure S7 the reported experimental performance in specific energy, specific power density, and efficiency of LiPo batteries [52] and CO_2 canisters [8] typically used to power untethered soft robots, in blue and green, respectively. We compare available data from literature

of different energy storage strategies with our thermopneumatic energy harvesting and storage approach (represented as a red star) in Figure S7. We measure a specific energy density of $\approx 112.6\frac{\text{J}}{\text{kg}}$ and a specific power density of $\approx 2.7\frac{\text{W}}{\text{kg}}$, calculated using the 42s discharge time we have recorded in Figure 5 during the indoor locomotion experiments.

From this comparative study, we observe that the different methods we report for energy autonomy can span several orders of magnitude for what concerns specific energy density, specific power density and efficiency. Some methods, such as explosion-based devices, can produce specific power density orders of magnitude higher than all the other methods we studied. This is mainly due to the high energy density of the fuels used and the impulsive nature of the work that those systems can manifest. This is in contrast to systems based, for example, on phase transitions or on the release of gas through pressure regulators.

At the same time, CO_2 canisters demonstrate performances comparable to LiPo batteries in specific energy density, specific power density, and efficiency. However, this is due to the high pressure in such pressurized stiff volumes (~ 60 bar). A few orders of magnitude separate LiPo batteries and CO_2 canisters from pneumatic, chemical reaction, explosion, and phase-transition-based devices. Clearly, for all such systems, the most suitable energy source solution must be found by interpolating energy and power requirements with total weight and additional constraints, such as safety in, e.g., underwater environments, fire-hazard, and chemical toxicity.

For this reason, although we consider the analysis performed in Figure S7 to be representative for comparison, we acknowledge that there are fundamental differences, not only in energy autonomy strategies but also in initial purposes between the reported case studies.

A.8: Comparison with other LBF candidates

Our choice of Novec 7000 was made to study the use of LBF compatible with temperatures obtainable from heat exchange from natural environments during circadian oscillations. A well-detailed overview of different media can be found, e.g., in Figure S4 of [6], where saturation pressure and enthalpy of vaporization are studied in detail for different (low-boiling-point) fluids. Based on the thermodynamic properties of different LBFs candidates, we can comment on their potential for being used in our thermopneumatic energy strategy.

LBF masses: We emphasise that the number of moles and molar masses play a significant role in determining how much mass of LBF is needed. When considering the mass m, the number of moles n and the molar mass M follow the relation $m = nM$, we derive from the ideal gas law that:

$$p = \frac{nRT}{V} = \frac{mRT}{MV}.$$

As an example, given two chemical species with molar masses M_1 and M_2, $M_1 > M_2$ and masses m_1 and m_2, the same pressure can be achieved only if the same number of moles reaches the gaseous phase, namely

$$p = \frac{m_1 RT}{M_1 V} = \frac{m_2 RT}{M_2 V} \iff m_1 = m_2 \frac{M_1}{M_2}$$

Efficiency: We can leverage the model in Equation S12 to get insights into how efficiency would change if different powering media are used. In particular, for this study, we focus on acetone, ethanol, and water as they are potential alternatives for environmental applicability. Nevertheless, to reach the evaporation threshold at ambient temperature and instantiate the compression phase, higher temperatures are needed. The increase in operating temperature affects the overall Carnot efficiency of the system as well. Following the data reported when

comparing such LBFs in Figure 3 of [6], and assuming we target to reach the same triggering pressure of 35kPa, we observe that our model in Equation S12 yields:

Acetone

- T for reaching 35kPa $= 85^{\circ}$C
- $m_{\text{acetone}} = 17$g
- $\eta_{\text{acetone}} \approx 0.12\%$, $\eta_{\text{Carnot, acetone}} \approx 12.4\%$
- $\frac{\eta_{\text{acetone}}}{\eta_{\text{Carnot, acetone}}} \approx 0.96\%$

Ethanol:

- T for reaching 35kPa $= 95^{\circ}$C
- $m_{\text{ethanol}} = 21.5$g
- $\eta_{\text{ethanol}} \approx 0.08\%$, $\eta_{\text{Carnot, ethanol}} \approx 17.3\%$
- $\frac{\eta_{\text{ethanol}}}{\eta_{\text{Carnot, ethanol}}} \approx 0.46\%$

Water:

- T for reaching 35kPa $= 110^{\circ}$C
- $m_{\text{water}} = 55$g
- $\eta_{\text{water}} \approx 0.08\%$, $\eta_{\text{Carnot, water}} \approx 22.7\%$
- $\frac{\eta_{\text{water}}}{\eta_{\text{Carnot, water}}} \approx 0.35\%$

For a better comparison, we recall that in our case study (using the highest value of efficiency from our model) we got:

Novec 7000 (our study):

- T for reaching $35\text{kPa} = 43^{\circ}\text{C}$
- $m_{\text{Novec 7000}} = 5\text{g}$
- $\eta_{\text{Novec 7000}} \approx 1.6\%$, $\eta_{\text{Carnont, Novec 7000}} \approx 6.32\%$
- $\frac{\eta_{\text{Novec 7000}}}{\eta_{\text{Carnot, Novec 7000}}} \approx 16\%$

Overall, our thermopneumatic strategy can operate at lower temperatures than the aforementioned LBF candidates. At the same time, using Novec 7000 a higher efficiency and ratio with corresponding Carnot efficiency can be reached.

Actuation frequency: A powering medium with lower thermal inertia (heat capacity, latent heat of vaporization) would yield a more reactive system. However, as we have seen in the case of the effects of moisture in Equation S15, given the masses of the powering and actuating media we use, we expect different LBF to affect only marginally the timescales for heating up and cooling down. As an example, for the LBF studied in [6], we can get a quantitative understanding of how much different thermodynamic properties of the system can affect the time scales of heating up and cooling down. For this analysis, we take into account specifically acetone, ethanol, and water as candidate powering fluids. When we take as reference values the latent heat of vaporization and heat capacity of Novec 7000 $L_{\text{Novec}} = 142\frac{\text{kJ}}{\text{kg}}$ and $c_{\text{Novec}} = 700\frac{\text{J}}{\text{kg}\cdot\text{K}}$, we can infer that $\frac{L_{\text{acetone}}}{L_{\text{Novec}}} \sim 3.7$, $\frac{L_{\text{ethanol}}}{L_{\text{Novec}}} \sim 5.8$, $\frac{L_{\text{water}}}{L_{\text{Novec}}} \sim 15.7$ and $\frac{c_{\text{acetone}}}{c_{\text{Novec}}} \sim 3.0$, $\frac{c_{\text{ethanol}}}{c_{\text{Novec}}} \sim 3.4$, and $\frac{c_{\text{water}}}{c_{\text{Novec}}} \sim 5.9$.Our simulation framework can help validate that, for the same valve design and environmental circadian oscillations in temperature and light intensity, alternative LBF candidates such as acetone or ethanol would not be able to produce pressures high enough to trigger the discharge phase. This incompatibility of alternative LBFs to operate under environmental

conditions is due to the combination of both higher heat capacity and boiling temperature. In our model, we consider that, given good agreement between the vapor pressure curve of Novec 7000 and our experimental data (Figure 3), the $p(T)$ follows the vapor pressure curve of acetone. We compare our experimental data and fit of vapor pressure in Figure 2b with the vapor pressure of acetone in Figure S8**a**. At the same time, we perform the study on different geographical locations we introduced in Figure 3**d** in Figure S8**b**. When considering the relative boiling temperature and heat capacity of acetone, we observe that the system would need temperatures of $\sim 85°$C in order to reach the firing threshold. On top of that, we observe that the system cannot reach the $T_{\text{boi}}(p_{\text{amb}}) = 56°$C, thus the evaporation threshold is never achieved, and fluctuations in pressure are due to the air volume inside the reservoir heating up, as we report in the simulations in in Figure S8**c**.

Such high temperatures are hardly ever compatibile with temperatures recorded in 2024 in the locations we highlight. At the same time, sunlight intensity is not sufficient to provide the additional required heat to bring the LBF the temperature necessary to trigger the discharge phase at 35kPa, as we show in Figure S8**c**.

Environmental applicability: It is worth mentioning that one major limitation of Novec 7000 is its global warming potential (100-year integrated time horizon, IPCC 2013) of $\text{GWP}_{\text{Novec}} = 530$. For a comparison, $\frac{\text{GWP}_{\text{acetone}}}{\text{GWP}_{\text{Novec}}} \sim 5 \cdot 10^{-4}$, while GWP tables focus on well-mixed, long-lived greenhouse gases, so we could not identify from literary sources $\text{GWP}_{\text{ethanol}}$, nor $\text{GWP}_{\text{water}}$, which we expect to be too low to be determined in the first place.This means that Novec 7000 can be considered extremely more pollutant as LBF then the aforementioned LBF candidates. This feature in particular prompted us to use utmost care and precautions during fabrication Novec 7000 (storing Novec 7000 in a refrigerated environment to prevent it from escaping the 3M container in its gaseous form, manipulating it always and only under a fume hood) while

preventing leakages and spills.

In conclusion, design changes are required to explore the use of different LBFs that could be more environmentally friendly while guaranteeing the same performances and applicability in open-world scenarios. We have updated the discussion of our article to include this additional information.

A.9: Strategies to reduce potential leakages of LBF

As for the leakages of LBF through the pouch, we consider the following arguments. To our knowledge, the long-term degradation of TPU in contact with Novec 7000 has not been quantified in the literature, and our early samples showed roughly unchanged pouch weight over about one year, although detecting small losses is difficult given the small LBF mass (5 g) relative to the pouch/connectors (≈ 30 g). To further reduce leakage, a practical alternative would be replacing the nylon-coated TPU pouch with a mylar (foil) balloon. Aluminised films (e.g., PET with a thin aluminium layer) provide a strong diffusion barrier that substantially lowers permeability, and they can be manufactured with heat-sealed seams similarly to our current pouches. Recent studies [1] have quantified that, by including aluminum foil, oxygen permeability can reach $0.7 \div 0.049 \text{cm}^3 \cdot \text{m}^{-2} \cdot$ day$\cdot$ atm, equivalent to $14 \div .8 \cdot 10^{-5}$L/day in our case study. As LBF molecules are larger than O_2 molecules, we expect these leakages to be even less pronounced when an aluminum coating is introduced in the design of the pouch.

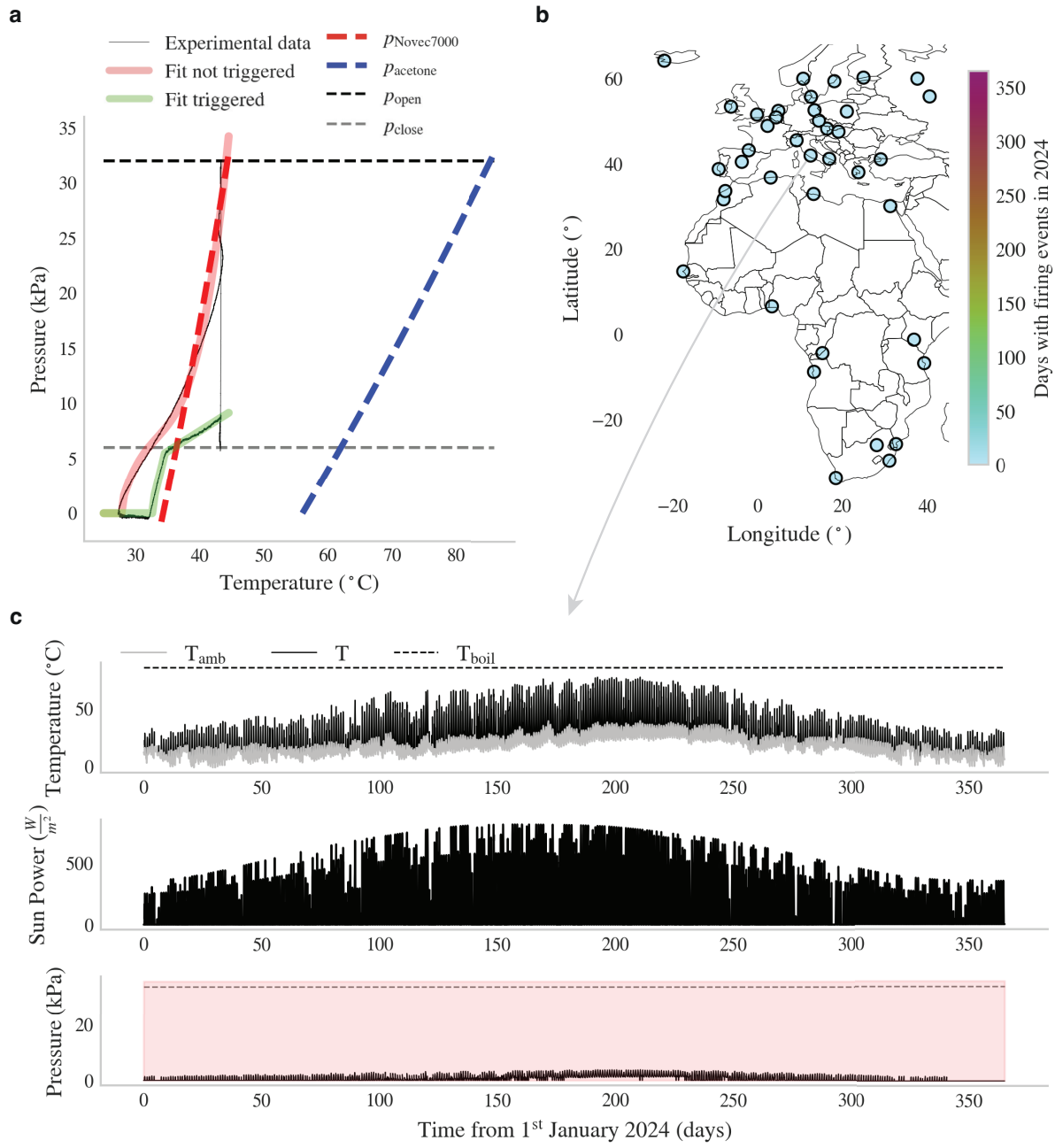

Figure S8: **Simulated experiment with acetone as LBF fluid.** **(a)** We compare the data in Figure 3**b** with the vapor pressure curve for acetone in (dashed blue). The ambient temperature necessary to reach the firing threshold at 35kPa while using acetone is now 85°. **(b)** By running the simulation on different locations during 2024 as in Figure 3**d** and using acetone thermodynamic properties, only a few firing events are achieved. **(c)** Example output data for the case of acetone as LBF in Rome throughout the whole 2024.

B: Heat transfer model

Our approach to model the heat transfer in our thermopneumatic cell is to consider the different subsystems of rigid air reservoir, LBF and air as a whole. To our knowledge, this approach has been only partially explored in literature [37] where, once the heat transfer equation has been defined, a fit on experimental data is performed to predict the response of pouch filled with LBF undergoing phase transition. Similarly, our approach first aims to identify the most significant contributions to heat transfer equations and fit the model to the observed results. Still, while performing this approximation, we inform our model with fundamental heat-transfer knowledge, based on convection, radiative losses, and light-intensity absorption.

We demonstrate that this simplification allows us to capture all the relevant features of the evolution in time t of the temperature $T(t)$ for given ambient temperature $T_{\text{amb}}(t)$ and incoming sun radiation $I(t)$. In our model for heat transfer, we include the different contributions to heat flux $\dot{Q}$ from convection, radiative losses, and absorption of sun radiation considering respectively the three following equations:

$$\dot{Q}_{\text{convection}} = A\,h\,(T(t) - T_{\text{amb}}(t)) \tag{S13a}$$

$$\dot{Q}_{\text{radiative losses}}(t) = A\,\epsilon\,\sigma\,(T^4(t) - T^4_{\text{amb}}(t)) \tag{S13b}$$

$$\dot{Q}_{\text{absorption}}(t) = \alpha\,A\,I(t) \tag{S13c}$$

in which A represents the surface area of the system, h the heat transfer coefficient, ϵ the emissivity of the system, σ the Stefan-Boltzmann constant and α a geometrical coefficient that accounts for projection effects due to the position of the sun during the day with respect to our system. In our model, we tune the coefficient for the heat transfer model using available data from the literature for transparent PET, so that we consider $h = 5.5\frac{\text{W}}{\text{m}^2\cdot\text{K}}$ [9], $\epsilon = .9$ [10, 11] and consider an area $A = 0.042\text{m}^2$ and $\sigma = 5.670 \cdot 10^{-8}\frac{\text{W}}{\text{m}^2\cdot\text{K}^4}$. By setting $\alpha < 0.5$, we impose that only half of the bottle is exposed to incident sun radiation while, for the sake of performing

a first-order approximation, we do not directly account for latitude and how α could change during the daylight hours due to the different relative position of the sun with respect with our system. Moreover, in our model we disregard contributions from advection as wind speed is negligible when considering elevation so close to ground level ($\mathcal{O}(10\text{cm})$), as in the case we show in our demonstrator in Supplementary Movie 1 [12]. Therefore, we model temperature changes in the system as

$$(m_{\text{air}}c_{\text{air}} + m_{\text{LBF}}c_{\text{LBF}})\frac{\mathrm{d}T(t)}{\mathrm{d}t} = -\dot{Q}_{\text{total}} = -(\dot{Q}_{\text{convection}} + \dot{Q}_{\text{radiative losses}} + \dot{Q}_{\text{absorption}}) \tag{S14}$$

where we used $m_{\text{air}} = 1.293\text{g}$ (mass of 1L of air), $m_{\text{LBF}} = 5\text{g}$ as from our experiments and heat capacities $c_{\text{air}} = 700\frac{\text{J}}{\text{kg}\cdot\text{K}}$ and $c_{\text{LBF}} = 1300\frac{\text{J}}{\text{kg}\cdot\text{K}}$ for air and LBF respectively.

To calibrate the value of α that could fit the values we observe in the experimental realization of our system, we consider the outdoor experiment in Figure 4. During the outdoor experiment, we visually access information from pressure, we gather data from local weather stations, reproduce the experimental conditions in simulation, and fit α to the experimental observations. In particular, we consider that, starting from T_{lab}, the system took $\simeq 2$ hours to reach the opening pressure. Therefore, we choose $\alpha = 0.275$ value that returns a similar time scale for reaching the firing pressure, giving the experimental condition. We report the effect of different α in Figure S9 on the simulated data from the same day and location as the one experimentally probed in Figure 4 for the outdoor experiment. From these simulations, we observe that the different α yield different contributions to the heat transfer, following from Equation S13**c** as we report in Figure S9**a**-**b**. This has direct consequences on $p(t)$ that, in our model, solely depends on air temperature $T(t)$ and $F(t)$ firing state.

Following the description we provided while presenting the model in Figure 3**b**, we report the different values of $p(t)$ associated with the corresponding α values in Figure S9**c**.

Moreover, from experimental observations in Figure S17**b**, we observe that an opening event

does not significantly affect the temperature inside the air reservoir. Therefore, in our model, the air pressure $p(t)$ is a function of temperature $T(t)$ and firing state $F(t)$ whereas we consider $T(t)$ not to be affected by $p(t)$ nor $\dot{p}(t)$.

To evaluate air pressure, we perform a fit on the data in Figure 3**b** using a cubic function for $F = false$ and a piecewise linear function for $F = true$. We gather weather data through `meteodata` Python package to access *National Oceanic and Atmospheric Administration* (NOAA) and *Deutscher Wetterdienst* (DWD) historical database of temperatures $T_{\text{env}}(t)$, `solarpy` and `meteostat` Python libraries to access data on sun intensity, comprehensive of how cloud coverage affects oscillations in solar power on ground, at any given location in time. Since the air heat capacity increases with absolute humidity H [13],

$$c_{\text{air}} = c_{\text{V,air}} + 1820H \ \frac{\text{J}}{\text{kg} \cdot \text{K}}, \tag{S15}$$

we extended the model accordingly. However, because the air mass in the 1 L cell ($m_{\text{air}} = 1.293\,\text{g}$) is small compared to the LBF mass ($m_{\text{LBF}} = 5\,\text{g}$, $c_{\text{LBF}} = 1300\frac{\text{J}}{\text{kg}\cdot\text{K}}$), the system's thermal inertia is dominated by the LBF, and incorporating Equation S15 yields only marginal changes in the simulation results.

To better highlight how seasonal changes in temperature and sunlight exposure can affect the amount of environmental energy that can be harvested by our proposed design, in Figure S10 we report an example of output throughout the whole 2024 in Toulouse and Rome. Also, in this case, we observe that, although ambient temperature is often not high enough to trigger our energy harvesting device, sunlight intensity can play a major role in the energy balance to activate our system. This is particularly true when considering locations at different latitudes, e.g., by comparing Casablanca to Reykjavik.

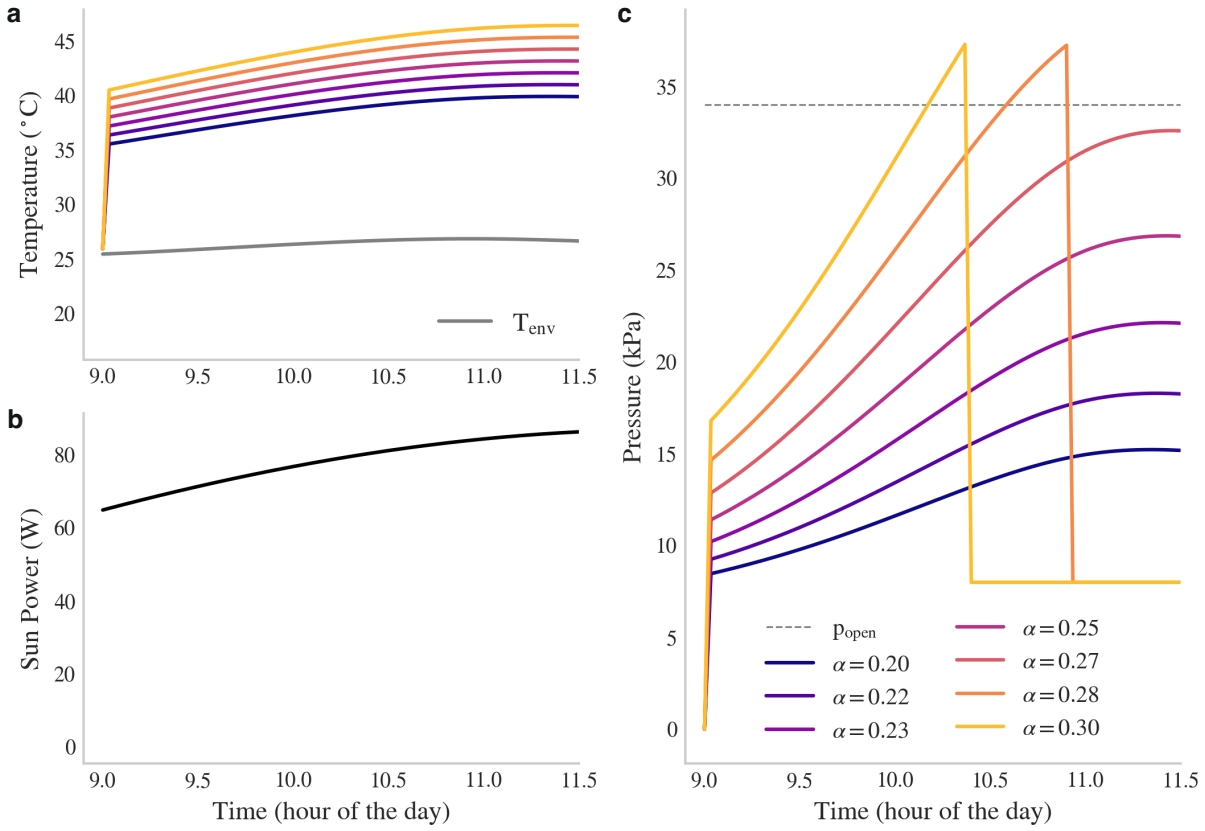

Figure S9: **Calibration simulation for the greybox model of heat exchange.** We gather weather data from the experiment performed on June 27th 2024 in Amsterdam and compare it with the numerical results from Equation S14. **(a)** Ambient temperature in gray and simulated air temperature inside the reservoir. **(b)** Power from sunlight intensity impinging on part of the surface of the air bottle. **(c)** Simulated pressures. In **a** and **c** we represent with different colors the simulations performed for increasing values of α in Equation S13**c**, to visualize their effect on $p(T)$.

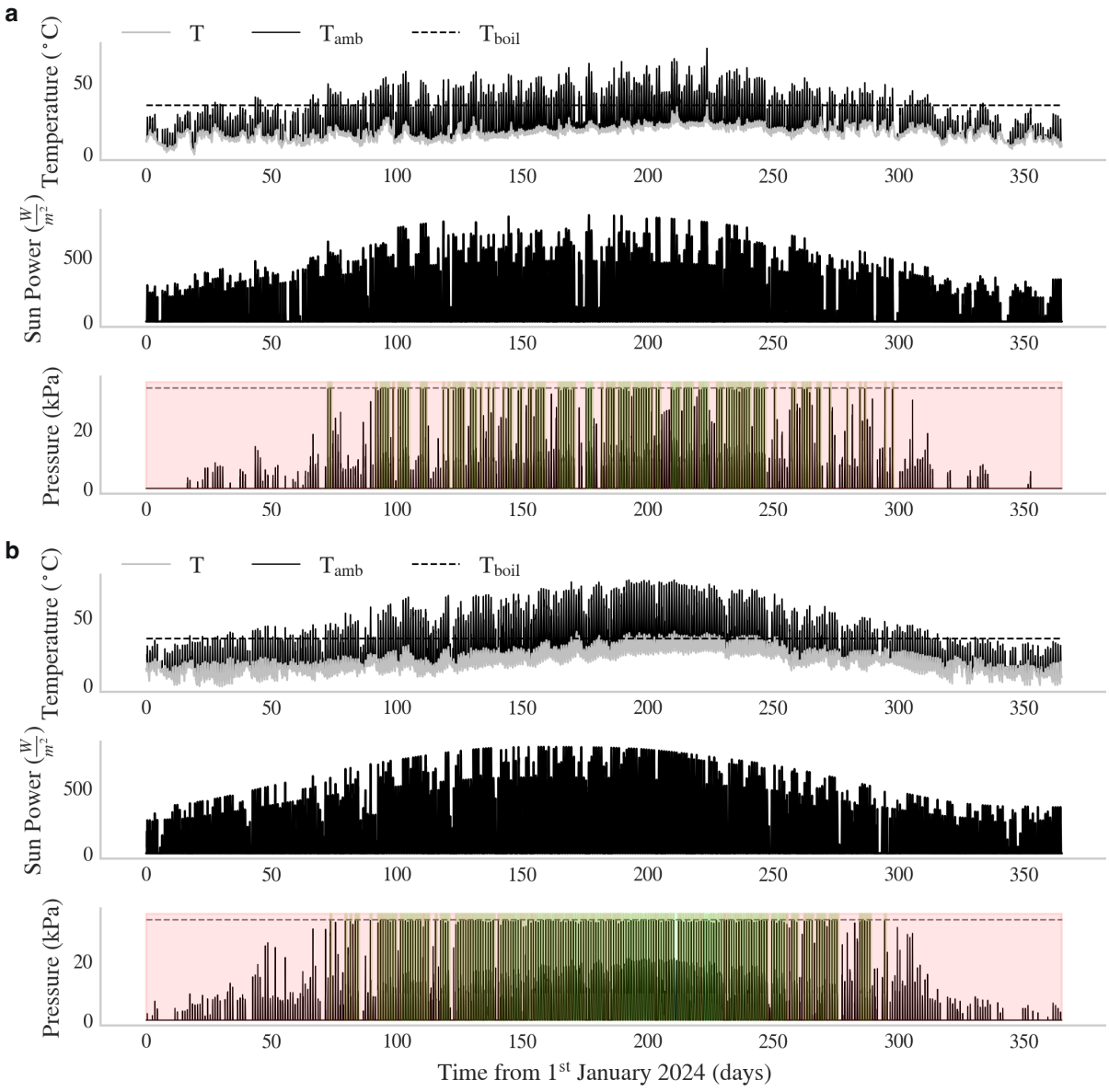

Figure S10: **Simulation output examples based on historic weather data at different location.** Example output from the model for the thermopneumatic response of our energy harvesting system throughout 2024. We report temperatures, solar power and pressure for two example cases in **(a)** Toulouse and **(b)** Rome. The dashed line in the pressure plots represents the opening pressure of the pressure relief valve, while the green color represents the occurrence of a firing event, just like in Figure 3**c**.

B1: Effect of wind on heat transfer

We conduct an additional analysis based on intuitions from the literature to first estimate wind speed at the height of interest based on known local features of the testing area, and then use them in our heat transfer model. To model the wind speed U at z height from the ground, we use a logarithmic wind profile, as is standard in the literature[14, 15]

$$U(z) = \frac{u_*}{\kappa} \ln\left(\frac{z}{z_0}\right), \tag{S16}$$

where u_* is the so-called friction velocity, κ, the von Kármán constant (typically about 0.4), and z_0 is the aerodynamic roughness length [16]. To fit the parameters of this model to our experimental location, we leverage resources from the DTU Wind and Energy Systems. By fitting data with the logarithmic law in Equation S16, we infer $z_0 \approx 0.36$m, typically labelled as open terrain with short grass, which is compatible with similar measurements in suburban areas [17] that typically range between 0.3m and 1.5m. Results from the fit of the wind speed profile for different heights in the height range of interest are reported in Figure S11.

The profile we report in Figure S11, in combination with our experimental intuitions while performing outdoor experiments, sufficiently validates that air speed in the boundary layer at less than 0.2m from the ground, where the experiment was performed, only has minor contributions to the heat transfer in our system.

To demonstrate the validity of this assumption, we assume a worst-case scenario where we consider the wind speed to be always 0.2m/s . For these results, we consider that for the case of windspeed lower than 3m/s, it is assumed that the convection coefficient increases linearly with wind speed [18]. Based on this widely accepted approximation [19, 20, 21], we assume that the

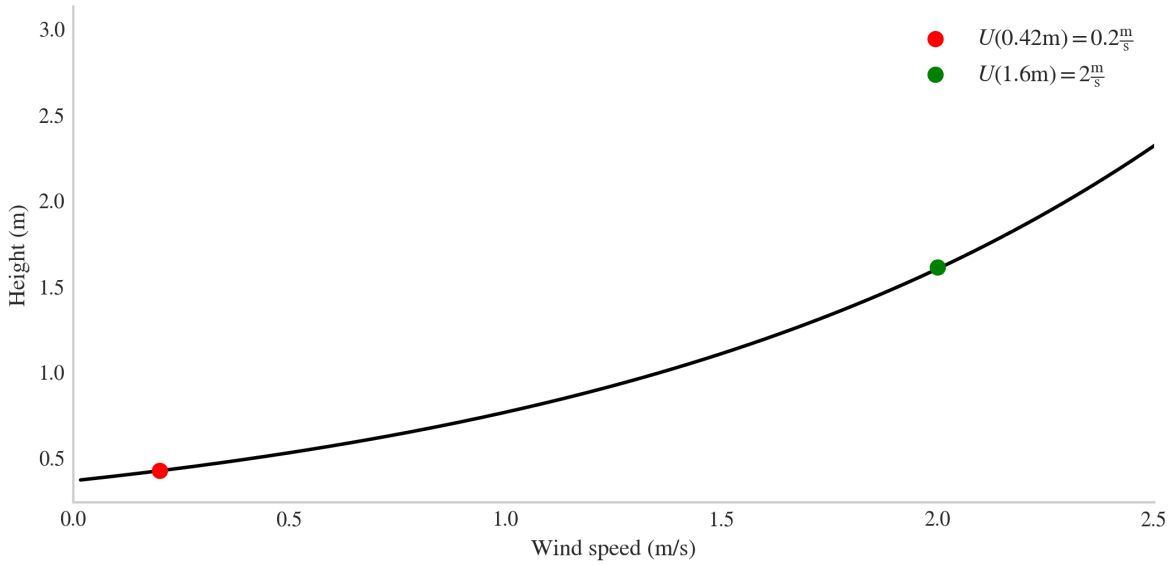

Figure S11: **Fit of logarithmic wind speed profile from Equation S16 with data extracted from the DTU Wind and Energy System website for Amsterdam on the day of the outdoor experiment.** Datapoint collected at heights of 10m, 50m, 100m, 150m and 200m were used to produce this fit, corresponding to a $z_0 = 0.36$m. The red and green dots relate to the $U(h)$ values corresponding to the analyses we perform in Figure S12.

convection coefficient h is influenced by wind speed following the relation

$$h(U) = h_0 + \left(3.8 \cdot \frac{Ws}{m^3 K}\right) U \tag{S17}$$

where $h_0 = 5.5 \frac{W}{m^2 K}$ is the baseline convection coefficient for the geometry of the thermopneumatic system, and U is the wind speed. This means that, in our worst-case scenario approximation, $h(U) = 6.45 \frac{W}{m^2 K}$ and $\frac{h(U)}{h_0} = 1.17$.

We report the comparison between the results of the model with the worst-case scenario approximation, with wind speed higher than the actual wind speed close to the system, and the results from Figure 3**d** in Figure S12 for data concerning Amsterdam. In particular, we observe that, even in this limit case where air convection is taken into account, the temperatures between the cases where wind speed is not considered (in blue) and taken into account (in red) are marginal. These subtle differences yield only minimal discrepancies in air pressure between the two cases. Globally, we observe that the temperature for the case of no convection is higher than that in the case in which air convection is considered.

Through this additional analysis, we observe that, in terms of modelling, even in the case of wind speed that is much higher and more uniform than what was experienced by our setup, the effect of wind speed has only a marginal influence on the occurrence of firing events. Through our modeling efforts, we demonstrate in Figure S12 that this statement holds unless the system is positioned at elevations from the ground that, for our case study, are ~ 10 times larger than the size of the system itself.

As a consequence of the limited influence of wind speed in our model, as well as the lack of uniform data for the different locations mapped in Figure 3**d**, we do not consider wind-related effects in the model we report in the main manuscript.

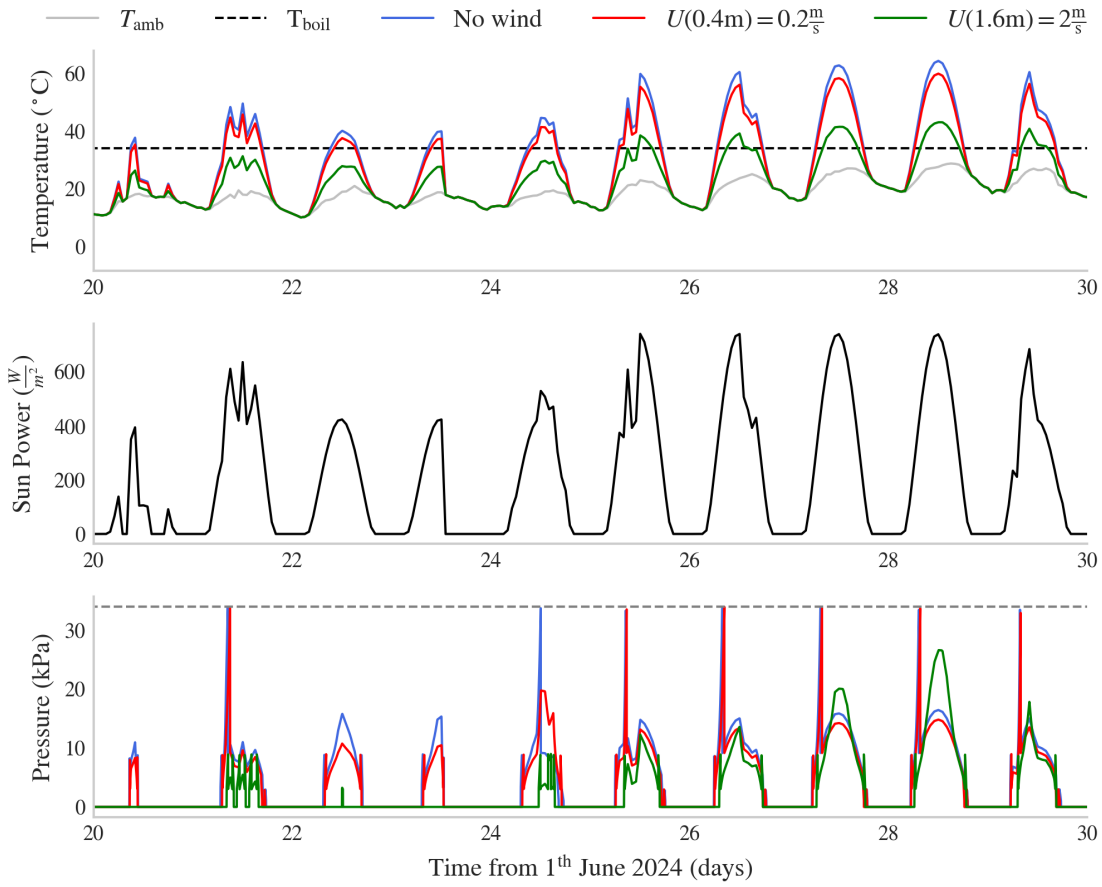

Figure S12: **Comparison between thermopneumatic models with and without effects of additional convection from wind speed under stronger-than-realistic wind speed in Amsterdam.** For these simulations, we use the same modelling framework used in Figure 3**d** with no wind (blue), and include a constant wind speed of $0.2\frac{\text{m}}{\text{s}}$ and $2\frac{\text{m}}{\text{s}}$ in red and green, respectively. For reference, the height of the demonstrator in Supplementary Movie 1 is < 0.2m, where wind speeds are close to null.

C: Figures for Methods

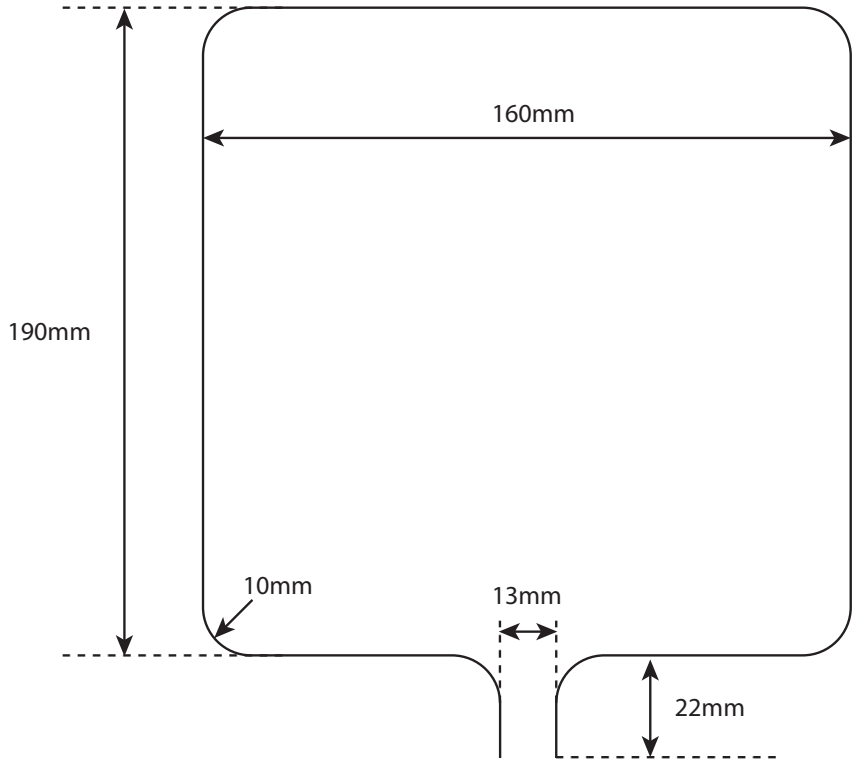

Figure S13: **Sketch of the heat-sealed pattern used to obtain the compliant TPU pouch to contain and isolate the LBF.** We use two sheets of Nylon, 70den, TPU-coated one side, 170g/sqm, sealing them at 270°C back to back so that the TPU sides face each other.

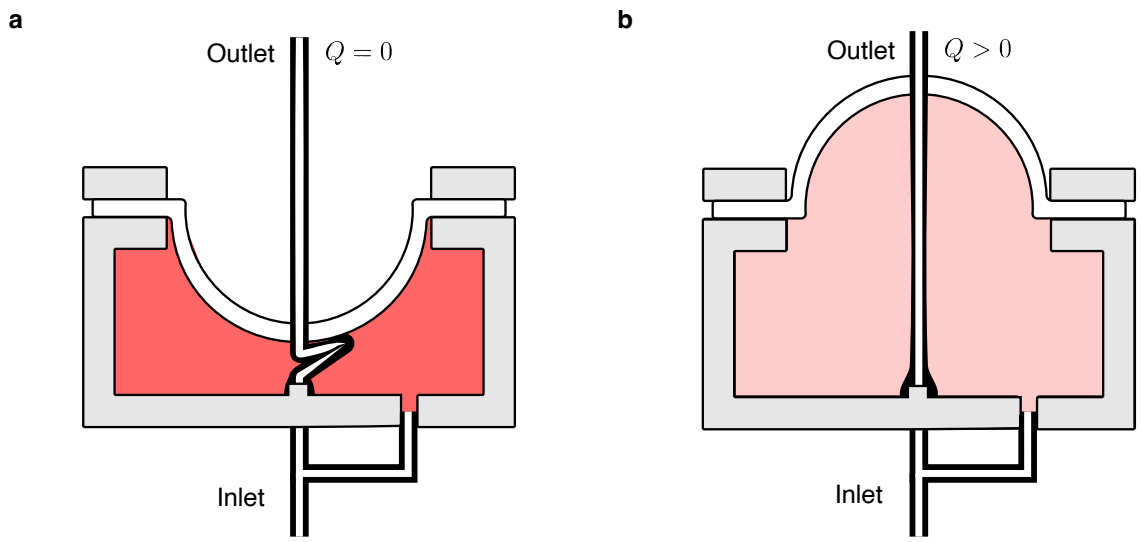

Figure S14: **Schematic representation of the working principles of the non-leaky pressure-release valve inspired by [48]. (a)** In the closed state, the silicone tube is kinked by the silicone dome as the air pressure at the inlet is not sufficient to snap the dome out of its stable configuration. **(b)** In the open state, the forces generated by the pressure on the inlet side cause the dome to snap, therefore unkinking the silicone tube and allowing positive air flow.

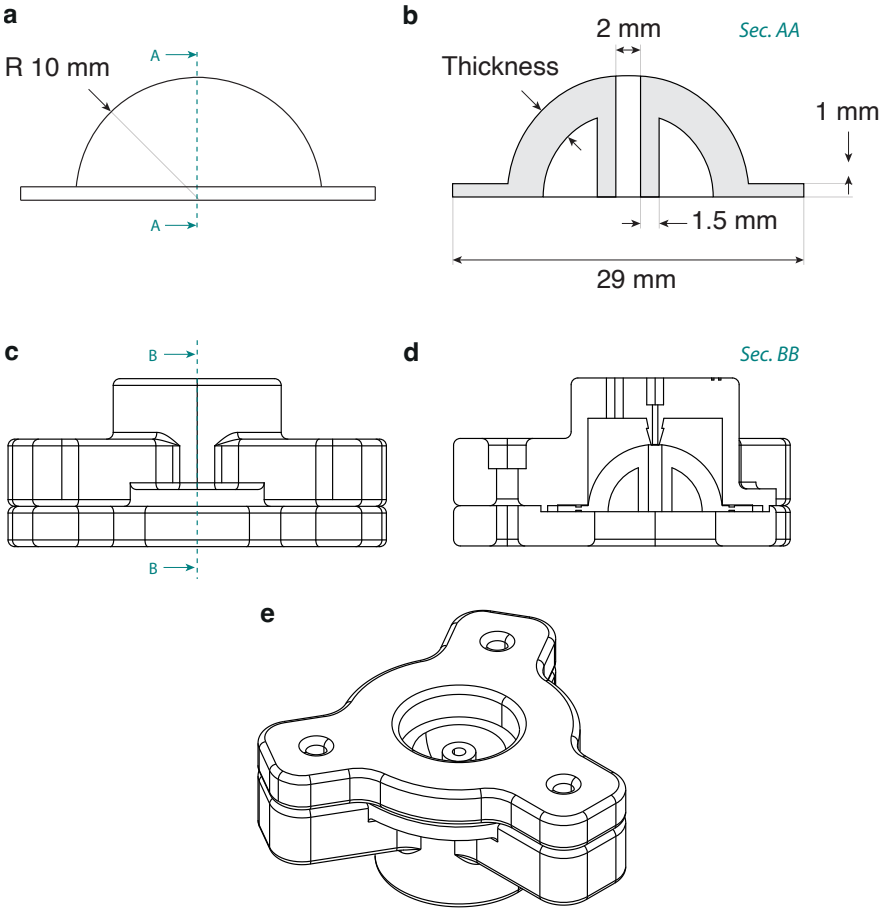

Figure S15: **Dimension of silicone dome and holder used to obtain the leakage-free pressure-release valve.** **(a)** Silicone dome size. **(b)** Cross section of silicone dome, highlighting its thickness and sizes of the channel passing through the pole of the dome. **(c)** Side view of the holder. **(d)** Cross-section view of the holder. **(e)** Isometric view of the assembled valve.

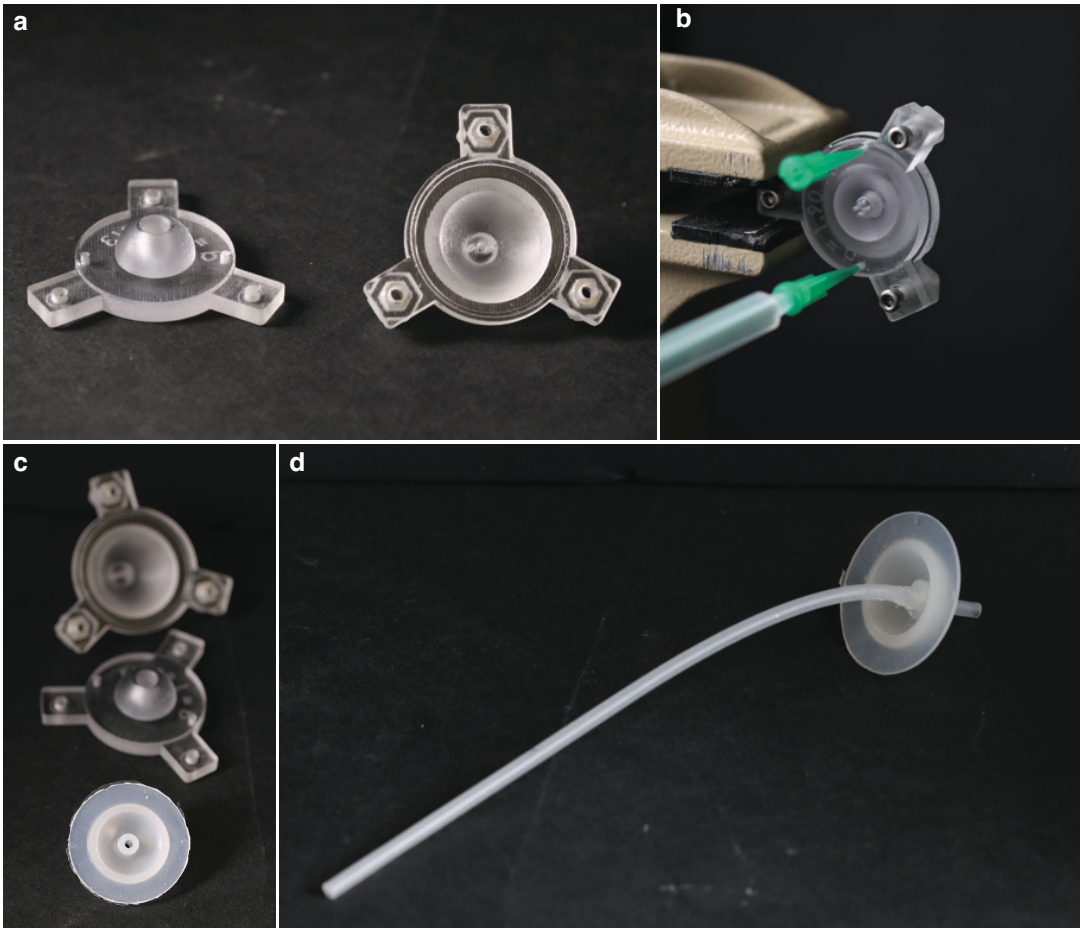

Figure S16: **Fabrication of the silicone dome structure used in the custom pressure-release valve.** Through injection molding of silicon, we obtain the dome structure with the parameters as in Figure S13. **(a)** Highlight of the top (left) and bottom (right) Veroclear molds used for the injection molding of Dragon Skin® 30 silicone. **(b)** Detail of injection molding process. Injecting silicone while holding the molds in the vertical position facilitates the escape of air bubbles that could compromise the functionality of the valve. **(c)** Veroclear molds and silicone dome after the 16 hours curing time. **(d)** Resulting structure after we slide the silicone tube inside the pole of the silicone dome and use SilPoxy® to seal the connection between the two on the concave side of the silicone dome.

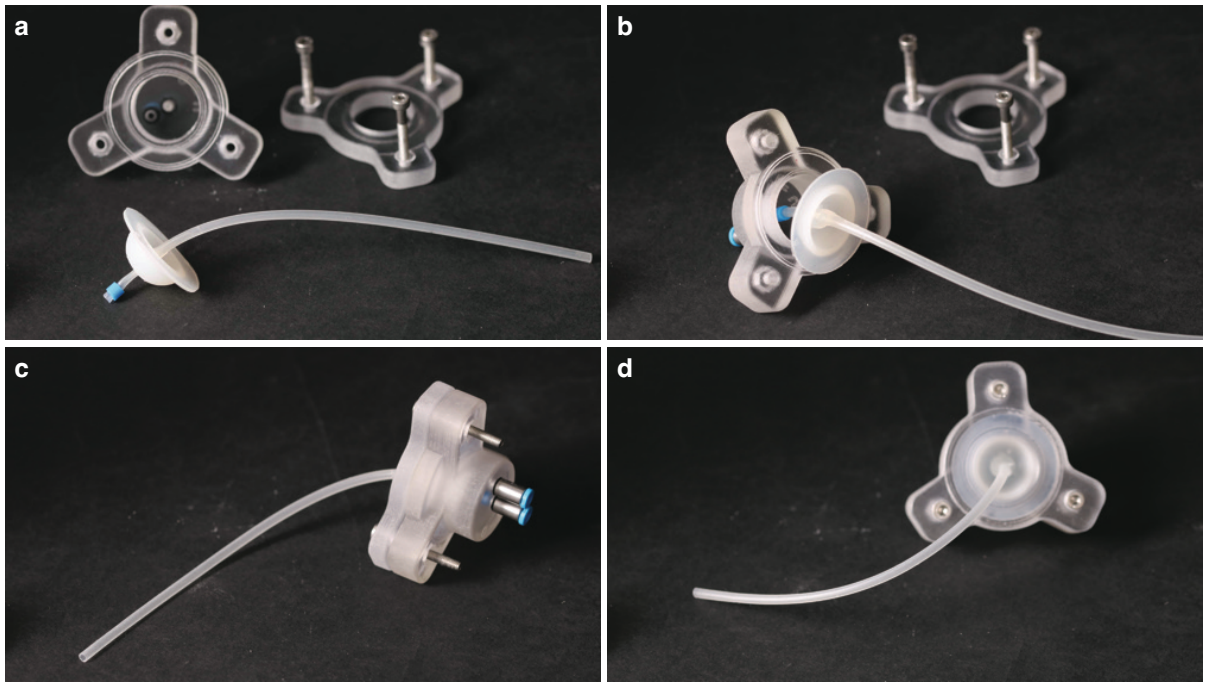

Figure S17: **Assembly of the pressure-release valve.** Starting from the component in Figure S14**d**, we assemble it using 3D printed holders with parameters as specified in Figure S13. **(a)** We place 2mm of FESTO® 4 tube on the end of the silicone tube connected to the bottom holder to guarantee a firm connection between the two. **(b)** We then slide the silicone tube on the bottom holder. **(c-d)** Inlet and outlet view of the assembled pressure-release valve.

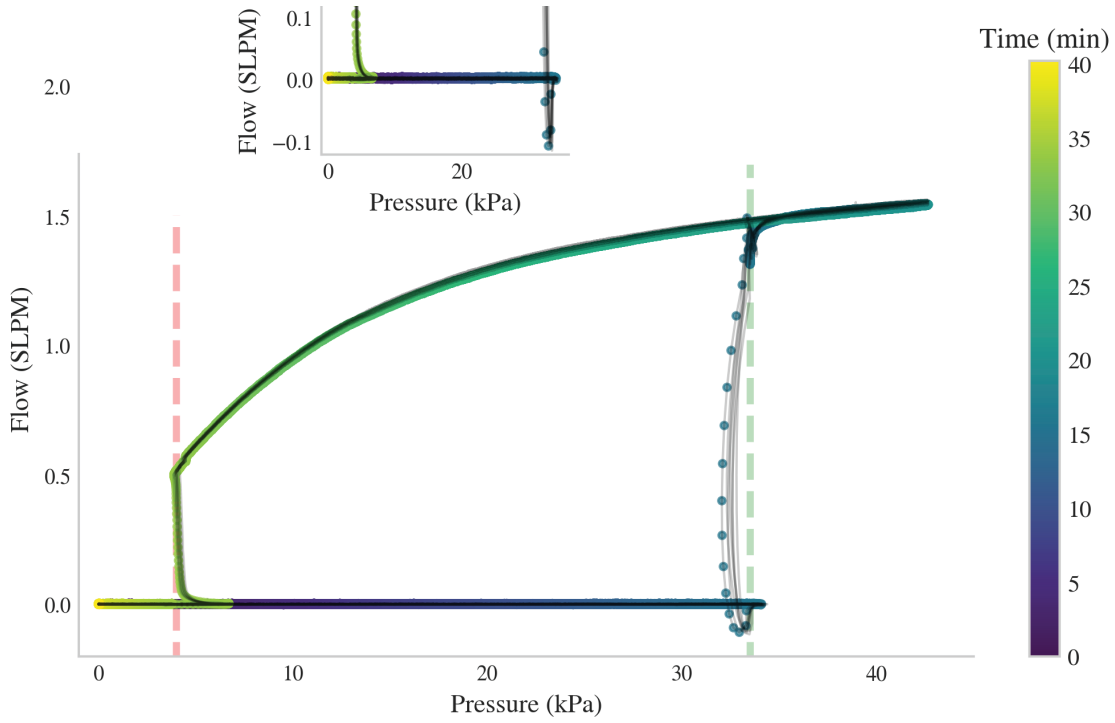

Figure S18: **Example data used to validate the presence of leakages in the pressure-release valve.** The black thin lines represent the measured data of the five continuous loops of pressurization and depressurization. The colored scatter plot represents the average of the values reached in the pressure-flow space over the time indicated. The dashed green and red lines represent the opening and closing pressures respectively. This data refers to the pressure-release valve with thickness $t = 1.9$mm used in the experiments in Figures 1-2-4-5.

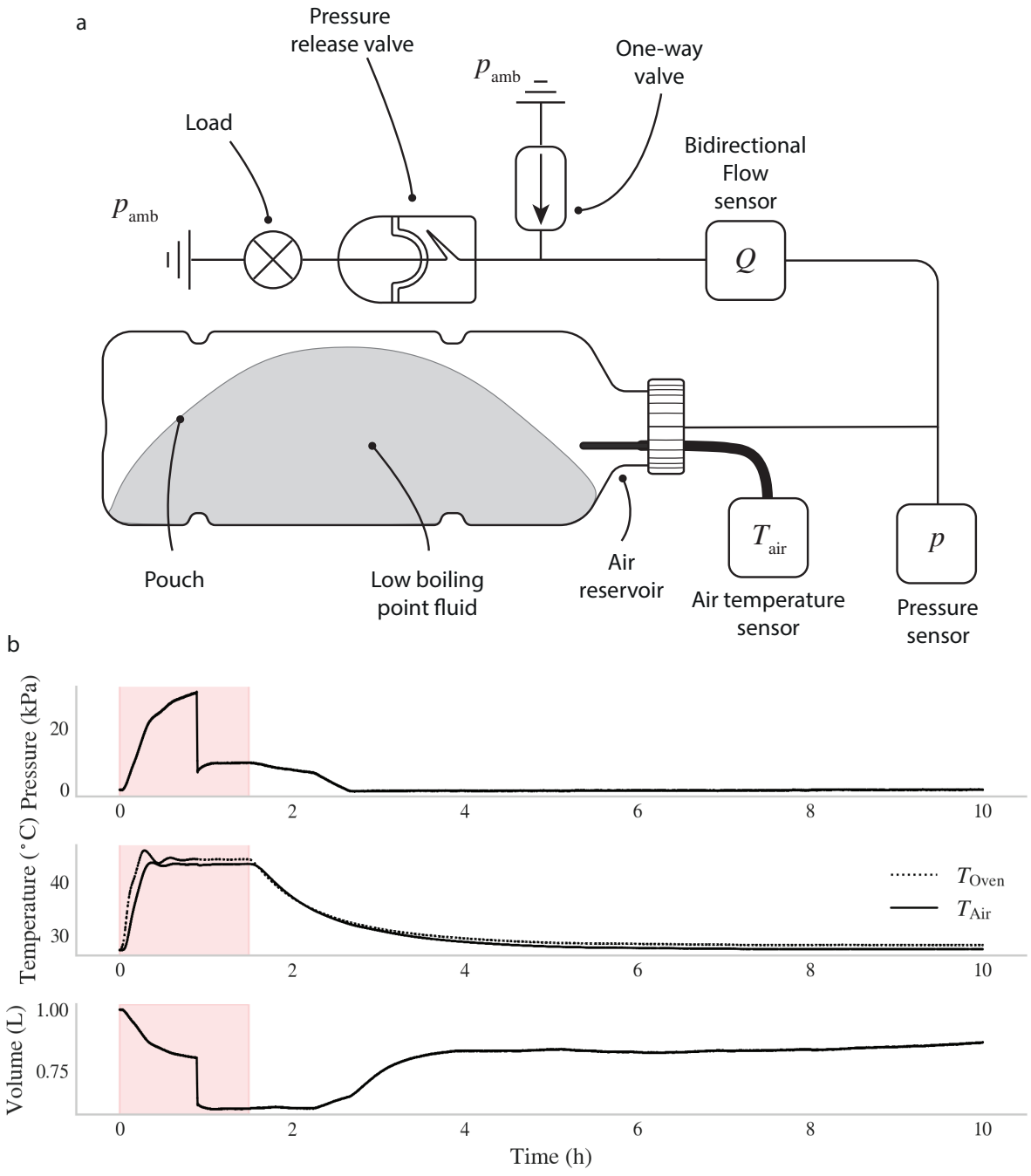

Figure S19: **Schematics of assembly for thermopneumatic measurements and example of data output in time**. (**a**) Thermopneumatic circuit with highlighted components and sensors. **(b)** Example of measured pressure and temperature data with inferred volume using Equations 4-7. We highlight in red the time span during which we regulate the oven temperature to 43°C.

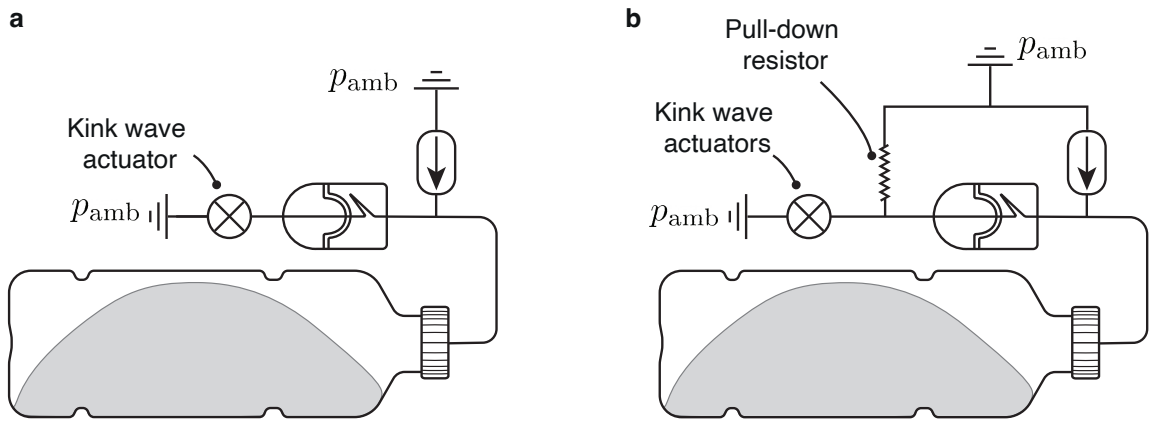

Figure S20: **Pneumatic circuits used in the demonstrators.** **(a)** Pneumatic circuit for the experiment performed outdoor in Figure 4. **(b)** Pneumatic circuit for the thermopneumatic walker demonstrator in Figure 5.

D: Description of Supplementary Movies

- **Supplementary Movie 1: Outdoor demonstrator** Movie of experimental execution of experiments presented for outdoor motion in Figure 4. At 9.15AM June 27th 2024, we brought the system outside the AMOLF building in Amsterdam and then connected it following the schematics in Figure S18**a**.

- **Supplementary Movie 2: Indoor locomotion demonstrators in laboratory environment** We assemble two self-oscillating actuators on the thermopneumatic cell as in Figure 5**a** and follow the pneumatic connections as in Figure S18**b**. To drive the temperature oscillations in our indoor locomotion demonstrators, we use a heat gun regulated at 220°C and progressively bring it closer to the setup to simulate an increase in temperature. In the first part of the movie, we report the experimental realization from which the data in Figure 5 has been extracted. In the second part of the movie, we repeat the indoor locomotion test controlling two consecutive thermopneumatic cycles and showing the potential for repeatability of the thermopneumatic loop for locomotion. After heating the system using the same protocol as in the first locomotion experiment in Figure 5, we wait 6 hours to let the system undergo its recharge phase before repeating the same heating procedure.

E: Table of fluidic setup details

Reference (Sampling Frequency)	Magnitude	Details
Figure 1**c**-**d** (1kHz)	p	Honeywell® SSCDRRN015PDAA5
	T_{oven}	LKMelectronic® 224 , PT100
	T_{air}	LKMelectronic® 224 , PT100
	Flow In	Honeywell® AWM5000-5SLPM
	Flow Out	Honeywell® AWM5000-15SLPM
	Load	VWR® Luer 22 Gauge Needle
Figure S4 (100Hz)	p	Honeywell® SSCDRRN015PDAA5
	T_{oven}	LKMelectronic® 224 , PT100
	T_{air}	LKMelectronic® 224 , PT100
	Flow In	Honeywell® AWM5000-5SLPM
	Flow Out	Honeywell® AWM5000-15SLPM
	Load	VWR® Luer 22 Gauge Needle
Figure 4	p	FESTO® Analog Pressure gauge
Figure 5 (50Hz)	T	Flir® I60
	Distance	ArucoTracking
	Pull-down Resistor	VWR® Luer 21 Gauge Needle
Figure S1(1kHz)	p	Honeywell® SSCDRRN015PDAA5
	T_{oven}	LKMelectronic® 224 , PT100
	T_{air}	LKMelectronic® 224 , PT100
Figure S2 (1kHz)	p	Honeywell® SSCDRRN015PDAA5
	T_{oven}	LKMelectronic® 224 , PT100
	T_{air}	LKMelectronic® 224 , PT100
	Flow In	Honeywell® AWM5000-5SLPM
	Flow Out	Honeywell® AWM5000-15SLPM
	Load	VWR® Luer 22 Gauge Needle
Figure S5 (1kHz)	p	Honeywell® SSCDRRN015PDAA5
Figure S16 (1kHz)	p	NXP® MPX5100DP
	Flow	Honeywell® AWM5000-5SLPM
Figure S17 (1kHz)	p	Honeywell® SSCDRRN015PDAA5
	T_{oven}	LKMelectronic® 224 , PT100
	T_{air}	LKMelectronic® 224 , PT100
	Flow In	Honeywell® AWM5000-5SLPM
	Flow Out	Honeywell® AWM5000-15SLPM
	Load	VWR® Luer 22 Gauge Needle

Table S1: **Details of experimental setup components**

F: References in Supplementary Material

References

[1] J. Wang, *et al.*, Hybrid films with excellent oxygen and water vapor barrier properties as efficient anticorrosive coatings, *RSC Advances* **8**, 21651–21657 (2018).

[2] R. F. Shepherd, *et al.*, Using explosions to power a soft robot, *Angewandte Chemie International Edition* **52**, 2892–2896 (2013).

[3] C. A. Aubin, *et al.*, Powerful, soft combustion actuators for insect-scale robots, *Science* **381**, 1212–1217 (2023).

[4] M. A. Bell, B. Gorissen, K. Bertoldi, J. C. Weaver, R. J. Wood, A modular and self-contained fluidic engine for soft actuators, *Advanced Intelligent Systems* **4** (2021).

[5] S. D. Gollob, *et al.*, *2025 IEEE 8th International Conference on Soft Robotics (RoboSoft)* (IEEE, 2025), p. 1–8.

[6] D. Fonseca, P. Neto, Electrically-driven phase transition actuators to power soft robot designs, *Nature Communications* **16** (2025).

[7] L. F. Gockowski, C. Xiao, A. Hao, Y. Zhu, B. Liao, M. T. Valentine, and E. W. Hawkes, "Improving the Efficiency of Soft Phase-Change Actuators Using Thermodynamic Analysis," *Soft Robotics*, vol. 12, no. 6, pp. 687–697, Dec. 2025.

[8] M. Adami, A. Seibel, On-board pneumatic pressure generation methods for soft robotics applications, *Actuators* **8**, 2 (2018).

[9] A. Liga, *et al.*, Study on heat transfer coefficients during cooling of pet bottles for food beverages, *Heat and Mass Transfer* **52**, 1479–1488 (2015).

[10] B. Saggin, *et al.*, Non-contact measurement of the temperature profile of pet preforms, *Measurement* **133**, 412–420 (2019).

[11] D. Meng, *et al.*, Polyethylene terephthalate-based colored emitters for efficient daytime radiative cooling, *Results in Physics* **46**, 106254 (2023).

[12] J. C. Wyngaard, Book review: Atmospheric turbulence. models and methods for engineering applications by hans a. panofsky and john a. dutton, *AIAA Journal* **23**, 2008–2009 (1985).

[13] Y. A. Cengel, M. A. Boles, *Thermodynamics: An Engineering Approach* (McGraw-Hill Professional, New York, NY, 2014), 8th edn.

[14] G. Hellmann, "Über die Bewegung der Luft in den untersten Schichten der Atmosphäre: Erste Mitteilung," in *Sitzungsberichte der Königlich Preußischen Akademie der Wissenschaften: Jahrgang 1914, Erster Halbband Januar bis Juni*, 1914.

[15] S. Wan, L. Chen, S. Jin, W. Yin, Y. Cui, and F. Zhang, "Estimates of Wind Speed Profiles from Surface Observations: Machine Learning Versus Monin–Obukhov Approach," *Boundary-Layer Meteorology*, vol. 191, no. 2, 2025. doi: 10.1007/s10546-025-00903-2.

[16] H. Tennekes, "The Logarithmic Wind Profile," *Journal of the Atmospheric Sciences*, vol. 30, no. 2, pp. 234–238, Mar. 1973. doi: 10.1175/1520-0469(1973)030¡0234:TLWP¿2.0.CO;2.

[17] J. C. Kaimal and J. J. Finnigan, *An Introduction to Boundary Layer Meteorology*. Dordrecht, The Netherlands: Springer, 1988. doi: 10.1007/978-94-009-3027-8.

[18] A. Rahmani, F. Chouaf, L. Bouzid, and S. Bedoui, "Experimental evaluation of the wind convection heat transfer on the glass cover of the single-slope solar still," *Heat Transfer*, vol. 53, no. 3, pp. 1292–1311, Jan. 2024. doi: 10.1002/htj.22997.

[19] S. Kumar, V. B. Sharma, T. C. Kandpal, and S. C. Mullick, "Wind induced heat losses from outer cover of solar collectors," *Renewable Energy*, vol. 10, no. 4, pp. 613–616, Apr. 1997. doi: 10.1016/S0960-1481(96)00031-6.

[20] S. Sharples and P. S. Charlesworth, "Full-scale measurements of wind-induced convective heat transfer from a roof-mounted flat plate solar collector," *Solar Energy*, vol. 62, no. 2, pp. 69–77, Feb. 1998. doi: 10.1016/S0038-092X(97)00119-9.

[21] S. Kumar and S. C. Mullick, "Wind heat transfer coefficient in solar collectors in outdoor conditions," *Solar Energy*, vol. 84, no. 6, pp. 956–963, Jun. 2010. doi: 10.1016/j.solener.2010.03.003.